# Synthesis and Characterization of Magnetic Nanocomposites and Their Applications Study

**Changyong Lu**

Universitat Autònoma de Barcelona

PhD Thesis 2017

# Synthesis and Characterization of Magnetic Nanocomposites and Their Applications Study

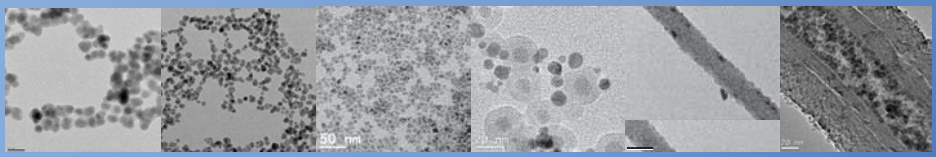


Author: Changyong Lu

Supervised by:

Prof. Josep Ros Badosa

Dr. Susagna Ricart Miro

PhD. Program in Materials Science

Chemistry Department-UAB


ICMAB

CSIC


PhD Thesis 2017

# Synthesis and Characterization of Magnetic Nanocomposites and Their Applications Study

Author: Changyong Lu

Supervised by:

Prof. Josep Ros Badosa

Dr. Susagna Ricart Miro

PhD. Program in Materials Science

Chemistry Department-UAB


Prof. Josep Ros Badosa, professor of the on the inorganic chemistry of Universitat Autònoma de Barcelona (UAB) and Dr. Susagna Ricart Miro, tenured scientist of Materials Science Institute of Barcelona (ICMAB)

Certify

That the dissertation **"Synthesis and Characterization of Magnetic Nanocomposites and Their Applications Study"** submitted by Mr. Changyong Lu to the Sciences Faculty in fulfillment of the requirements for the Doctor of Philosophy degree in the Materials Science program has been performed under their supervision.

Prof. Josep Ros Badosa
Chemistry Department
Universitat Autònoma de Barcelona (UAB)

Dr. Susagna Ricart Miro
Materials Science Institute of Barcelona (ICMAB)

Bellaterra, Barcelona (Spain), 6th June 2017

# Acknowledgements

I would like to show my greatest appreciate to all the people and institutions, I cannot make this thesis possible without your help.

First, I would like to express my deep gratitude to my supervisors Prof. Josep Ros and Dr. Susagna Ricart for providing me this valuable opportunity to study in Universitat Autònoma de Barcelona (UAB) and Materials Science Institute of Barcelona (ICMAB). The experience of this PhD study will be one of my most precious memory in my life. Very special acknowledgements to my supervisors for your continuous patience, advice, generous support and chance to collaboration with other research groups during my PhD study. Your knowledge and discussions about chemistry science are essential to the accomplishment of my thesis.

I would like to thank the Spanish Government, the Generalitat de Catalunya and the European Union for the financial support to the research project. Special thanks must be given to Chinese Scholarship Council (CSC) for giving me the 4 year PhD grants which is critical factor for my study in Spain.

This work would not have been finished with the collaboration and interaction with other research groups and experts in various fields.

I would also like to give my gratitude to Dr. Gerard Tobias and Dr. Sandoval Rojano Stefania for your direction about carbon nanomaterials research. Thank you so much for providing me the

carbon nanomaterials and teaching me about carbon materials science. Very special thanks will also be given to Prof Carme Nogués and Antonio Aranda-Ramos for your great help about cytotoxity study and interaction with cells about my core-shell nanoparticles which give me the hope about using this materials in biology research. I would also like to thank Prof José Luis Bourdelande Fernández for providing me the idea about decoration core-shell nanoparticles with MC540 molecules. Appreciation must be given to Dr. María Isabel Pividori and Laura Martinez for the good cooperation and direction about my research on core-shell nanoparticles application in biosensor. This work gives me a promising career plan for my future.

I would also like to express my deep gratitude to my colleagues in my group, especially to Alba Garzón Manjón, Natalia Chamorro, Jordi Martinez Esain and Dr. Ramon Yañez for helping me to get everything I need for my research work and your contribution to my daily life in Barcelona. Your guys gave a very unforgettable memory to me. To other members in superconducting materials and large-scale nanostructure group in ICMAB and inorganic chemistry department in UAB, for your help and wise advises about my PhD study.

This thesis would not have been finished without the fully characterization of my nanomaterials. I would like to thank Dr. Judit Oro in ICMAB and Dr. Emma Rossinyol in UAB for the assistance in the TEM test, Dr. Bernat Bozzo in ICMAB for helping me to do the SQUID test, Dr. Belén Ballesteros and Marcos Rosado in ICN2 for doing the EELS and EDS test for me. I would also like to appreciate the help from Dr. Angel Álvarez Larena in UAB for the XRD characterization, Mr. Ignacio Villarroya Antillac in UAB for the ICP test and Dr. Narcis Mestres in ICMAB for doing the Raman spectra experiments.

Here, I would also like to express my deep gratitude and love to my wife Wenjie Qian, thank you so much for your understanding, patience and support during all these years in every moment. Special thanks would also be given to my parents for their help and support during my PhD study.

Finally, thanks again to all your guys who did great contributions to my PhD and this unforgettable four years in Barcelona. It is my great pleasure to meet you, know you and have you in my life.

# Contents

# Abstract

Nanomaterials especially nanoparticles become one of the most attractive area not only in scientific research but also in industrial applications. In this thesis, the preparation of magnetite nanoparticles, their related nanocomposites and the application of those obtained nanomaterials have been studied.

The $Fe_3O_4$@$SiO_2$ core-shell nanoparticles were synthesized via normal and microwave assistance reverse microemulsion methods. The obtained nanoparticles were fully characterized with different laboratory techniques and the effect of reaction parameters on final products was also studied. These nanoparticles were used as a support of Ag catalysts nanoparticles and the as synthesized nanocomposites shown nice catalytic property and high recyclability.

A novel $Fe_3O_4$@GNF@$SiO_2$ nanocapsulates were also prepared via in situ formation of magnetite nanoparticles and silica coverage process. The obtained nanocapsulates have nice stabilities even in the acid environments. The potential application of these nanocapsulates in magnetic resonance imaging research was also studied.

On the other hand, the cytotoxity and interaction with cell of $Fe_3O_4$@$SiO_2$ core-shell nanoparticles were studied which indicate the possibility of using them in biomedical research. Then, the $Fe_3O_4$@$SiO_2$ core-shell nanoparticles were further decorated with biomolecules such as MC540 and L-thyroxine. The $Fe_3O_4$@$SiO_2$ core-shell nanoparticles with the surface functionalized with molecule imprinted polymers also suggested the potential application in biosensor research.

# Abbreviations

3-methacryloxypropyltrimethyloxysilane MPS

(3-Aminopropyl)triethoxysilane APTES

Carbon nanotubes CNTs

Dimethylsulfoxide DMSO

Electron energy-loss spectrometry EELS

Energy dispersive X-ray analysis EDX

Ethylene glycol dimetacrylate EGDMA

Iron(III) acetylacetonate $Fe(acac)_3$

High angle annular dark-field scanning TEM HAADF-STEM

Hollow graphitized nanofibers GNF

Infrared spectroscopy IR

L-thyroxine L-T4

Magnetic resonance imaging MRI

Merocyanine 540 MC540

Methylthiazolyldiphenyl-tetrazolium-bromide MTT

Molecular imprinted polymer MIP

Nanoparticles NPs

Non-imprinted polymer NIP

Particles Ps

Scanning electron microscope SEM

Superconducting quantum interference devices SQUIDs

Tetraethyl orthosilicate TEOS

Tetrahydrofuran THF

Thermogravimetric Analysis TGA

Transmission electron microscopy TEM

Ultraviolet-Visible Spectroscopy UV-Vis

X-Ray Diffraction XRD

# Chapter 1 Introduction

## 1.1 Nanomaterials and nanoparticles

In recent decades, “nano” become a more and more widely used word in our life. This word comes from ancient Greek with the meaning of dwarf and now it is used to describe objectives with the order of magnitude $10^{-9}$ unites. Nanomaterials were defined as the materials with at least one spatial dimension less than 100 nm. Because of the promising applications in scientific research and industry area, lots of efforts have been applied in synthesize, control and functionalization works to obtain nanomaterials with outstanding properties which will make them do great contribution to our social welfare.

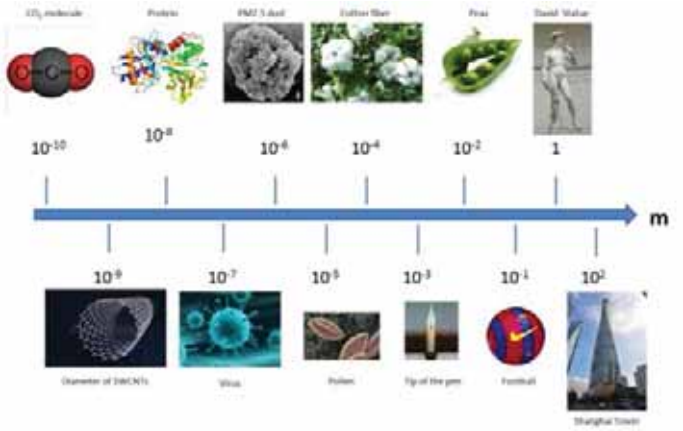


**Figure 1.1 Size scale from nano to the macroscopic world.**

# 1.1.1 Nanomaterials

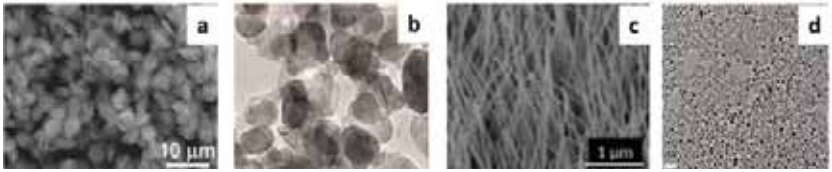


**Figure 1.2 SEM and TEM images of nanomaterials in different dimension (a) 3D, (b) 2D, (c) 1D and (d) 0D.[1-4]**

Nanomaterials could be classified according to their morphology. (see Figure 1.2)

**3D Nanomaterials:** Three-dimensional (3D) nanomaterials are always achieved by self-assembly of low-dimensional (0D, 1D or 2D) nanomaterials to complex structures such as hierarchical nanofibers and mesoporous flowerlike nanostructures[5, 6]. 3D nanomaterials are usually endowed with large specific surface areas in combination with unique physicochemical, electrical and catalytic properties[7, 8]. Moreover, the spatial configuration of the interconnected networks of building subunits in the 3D structures can further expand specific properties, such as efficient mass transport and charge carrier transfer[9], making the relevant materials popular with diverse applications[10].

**2D Nanomaterials:** The two-dimensional (2D) nanomaterials are thin films and interface with their thickness in a nanoscale for example graphene and $Ti_3C_2$ MXene layer[11]. These kinds of materials are prepared via chemical vapor deposition (CVD), pulsed laser deposition (PLD) or atomic layer deposition (ALD) processes. With the features of intrinsic quantum confined electrons, the 2D nanomaterials demonstrate a vast array of unique physicochemical properties,

such as planar conductivity, magnetic anisotropy, tunable band gap, and surface activity. Because of that, enormous efforts have been made to modify those intrinsic physical properties for the applications in high conductivity electrodes, planar spintronic and high-efficient photo-/electro-catalysis[12].

**1D Nanomaterials:** The one-dimensional (1D) nanomaterials include nanowires, nanotubes and nanorods[13] and they are synthesized by template-directed synthesis, electrospinning and 1D conjugation of building blocks[14]. Because of the fascinating properties such as electrical and electronic, piezoelectric and magnetic, catalytic, sensor as well as detector properties, coming from their atomic scale structures and their 1D morphology, the 1D nanomaterial have been identified as next generation building blocks for sensors, electronics, photonics and bioelectronics applications[15, 16].

**0D Nanomaterials:** The zero-dimensional (0D) nanomaterials are spherical particles that have three dimensions constrained on the nanoscale (usually 1–100 nm) which also named as nanoparticles or quantum dots[17]. Nowadays, 0D dimensional nanomaterials are of great scientific interest since they are the bridge between atomic and molecular structures and bulk materials and have many potential application in our society such as graphene quantum dots that could be used as electronic devices for bioimaging and photovoltaic application[18], or Au–$SiO_2$ core–shell nanoparticles applicable in Surface-enhanced Raman scattering (SERS) research[19].

## 1.1.2 Nanoparticles

Until now tremendous kinds of nanoparticles have been synthesized and applied in different fields. The nanoparticles can be classified according to their composition:

**Metal nanoparticles:** Organized from a cluster of metal atoms with the oxidation state equal to zero. Varieties of properties are presented in these nanoparticles for example electro confinement, plasmon resonance, etc[20, 21].

**Metal oxides:** This kind of materials are composed by metal oxides with special mechanical properties such as low elasticity, low hardness and high plasticity[22]. Beside of those mechanical properties, metal oxide nanoparticles also have many other functional properties for example $Fe_3O_4$ nanoparticles are superparamagnetic materials and can be used in magnetic manipulation[23], or $TiO_2$ nanoparticles that are the ideal candidate in water splitting for new generation energy research[24].

**Quantum dots:** Nanoparticles are composed generally by two or even more elements and at least one of them is metal element provide the gap between the conduction and valence band similar to a semiconductor material, some examples are CuS, PbS and CdSe[25, 26]. Due their special structures, quantum dots have great photoluminescence properties under ultraviolet light or other energy sources and this feature can be tuned by changing the shape and the size of quantum dots make them promising in many applications such as photocatalytic energy conversation[27] or multiplexed biosensors[28].

## 1.1.3 Properties of nanoparticles

Nanoparticles present different properties compared with bulk materials showing the opportunity to produce new kind of materials and devices for potential applications. These special characteristics come from their small size.

As all knows it, with the decrease size of one material its surface-volume ratio increases. The augmentation of the surface involves a significant increase of high reactive superficial unsaturated atoms with free atomic orbitals. This property makes nanoparticles to behave as functional materials. For example, Pt nanocrystals with specific surface have much higher catalytic properties in aromatization reactions than big size Pt particles[29], Shape controlled Ag nanocrystals have excellent current-carrying ability and low resistivity that make them interesting for electronic devices[30] and ferromagnetic nanoparticles (Co, Ni and Fe) with high magnetizations and coercitive fields have potential use as high-density storage media[31].

While in the counterpart, higher surface-volume ratio is related with higher surface tension, which is an undesirable energetic state for obtaining stable nanoparticles and leading to aggregations during the synthesis and further treatment of nanoparticles. In order to prevent the coalescence and maintain the size and properties of nanoparticles, several approaches can be used to stabilize nanoparticles. Surface of nanoparticles can be functionalised with capping ligand to produce a steric hindrance and geometric constrains[32]. The surface of nanoparticles could also be charged producing coulombic repulsion between each other resulting in stable nanoparticles system[33]. The combination of steric and electrostatic method (named ionic liquid) can also be used. In this

method, the liquid is formed by cations and anions which would electrostatically keep nanoparticles isolated, in the meanwhile the ionic liquid molecules are always have big structures generating steric hindrance between individual nanoparticles.

# 1.2 Magnetite nanoparticles

Over the past decades, $Fe_3O_4$ magnetite iron oxide nanoparticles have been investigated in depth because of the special magnetic properties coming from unpaired electrons in 3d orbitals of iron cations.

## 1.2.1 Magnetism

Generally speaking, magnetism is a physical phenomenon which certain materials show attraction or repulsion forces between each other. This property is the result of difference in the electronic configuration of different elements. According to their response to external applied magnetic field, materials can be sorted into the following groups.

**Nonmagnetic materials:** Materials with no magnetic reaction to the external applied magnetic field such as vacuum.

**Diamagnetic materials[34]:** These materials are weakly magnetic materials with the tendency to repulse themselves from the applied magnetic field. It is worth to point out that their electronic orbitals are full of paired electrons. (e.g. silver, lead, pyrolytic carbon)

**Paramagnetic materials[35]:** Materials have unpaired electrons whose magnetic vector is randomly oriented. When an external magnetic field is applied, the magnetic vector could be oriented. (e.g. palladium, tungsten or many first-row transition metal complexes)

**Ferromagnetic materials[36]:** These materials retain the magnetization in the absence of external magnetic field. The intrinsic magnetic moments of the materials have tendency to orient in the same direction. Therefore, these magnetic materials can be used as permanent magnets. (e.g iron, nickel and cobalt)

**Antiferromagnetic materials[37]:** These materials have zero magnetic moment and cannot produce magnetic field. Their intrinsic magnetic moments of neighbouring electrons are tending to orient in an opposite direction. It is worth to mention that, all the antiferromagnetic materials have a Neel Temperature, above which the antiferromagnetic materials would become paramagnetic materials. (e.g. nickel oxide, iron manganese alloy)

**Ferrimagnetic materials[38]:** These materials are like ferromagnetic materials which remain their magnetization in the absence of the external magnetic field. But their intrinsic magnetic moments are like antiferromagnetic materials, there are some electrons pointing to the opposite direction. (e.g. magnetite)

**Superparamagnetic materials[39]**: When the size of ferromagnetic and ferromagnetic materials decrease to a certain scale, they can act as a single magnetic domain and their magnetic moments are affected by thermal energy. As a result, they can be completely magnetized under a low magnetic field. (e.g. magnetite and cobalt ferrite nanoparticles with a very small size)

| Type | Example | Atomic/Magnetic Behaviour | | |
|---|---|---|---|---|
| Diamagnetic materials | Inert gases; many metals eg Au, Cu, Hg; non-metallic elements e.g. B, Si, P, S; many ions e.g. $Na^+$, $Cl^-$ & their salts; diatomic molecules e.g. $H_2$, $N_2$; $H_2O$; most organic compounds | Atoms have no magnetic moment. Susceptibility is small & negative, $-10^{-6}$ to $-10^{-5}$ | 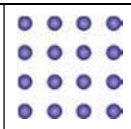 | 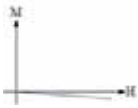  |
| Paramagnetic materials | Some metals, e.g. Al; some diatomic gases, e.g. $O_2$, NO; ions of transition metals and rare earth metals, and their salts; rare earth oxides. | Atoms have randomly oriented magnetic moments. Susceptibility is small & positive, $+10^{-5}$ to $+10^{-3}$ | 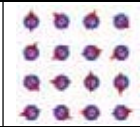 | 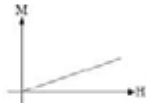  |
| Ferromagnetic materials | Transition metals Fe, H, Co, Ni; rare earths with $64 \leq Z \leq 69$; alloys of ferromagnetic elements; some alloys of Mn, e.g. MnBi, $Cu_2MnAl$. | Atoms have parallel aligned magnetic moments. Susceptibility is large (below TC) | 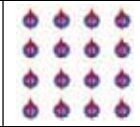 | 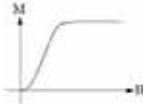  |
| Antiferromagnetic materials | Transition metals Mn, Cr & many of their compound, e.g. MnO, CoO, NiO, $Cr_2O_3$, MnS, MnSe, $CuCl_2$. | Atoms have antiparallel aligned magnetic moments. Susceptibility is small & positive, $+10^{-5}$ to $+10^{-3}$ | 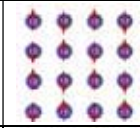 | 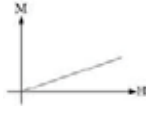  |
| Ferrimagnetic materials | $Fe_3O_4$ (magnetite); $\gamma$-$Fe_2O_3$ (maghemite); mixed oxides of iron and other elements such as Sr ferrite. | Atoms have mixed parallel and antiparallel aligned magnetic moments. Susceptibility is large (below TC) | 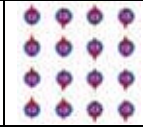 | 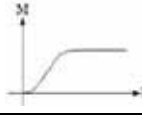  |

**Table 1 Summary of the different types of magnetic materials[40].**

# 1.2.2 Magnetite nanoparticles structure and properties.

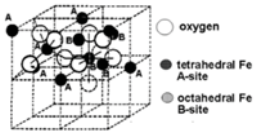


**Figure 1.3 Crystal structure of magnetite**

Magnetite is the iron oxide which displays a cubic inverse spinel crystal structure with Fd3m space group and α = 8.396Å. The close packing oxygen anions $O^{2-}$ form a face-centred cubic structure (fcc), $Fe^{2+}$ and half of $Fe^{3+}$ cations occupy the octahedral sites and the other half of $Fe^{3+}$ occupies the tetrahedral interstitial locations of the $AB_2O_4$ structure. The unit cell contains eight $Fe_3O_4$ molecules.

In the magnetic structure of magnetite, the orientations of the magnetic spin of cations located in octahedral positions are opposite to those in the tetrahedral sites which is the reason for their ferrimagnetic behaviour.

Due to their unique magnetic properties, magnetite nanoparticles have received tremendous attention is diverse research fields in catalysis, biosensor and bioimaging[41]. For example, Au coated magnetite nanoparticles could be used in bacteria detection[42], long-circulating heparin-functionalized magnetite nanoparticles are used as a nice protein drug delivery platform[43], photosensitizer functionalized magnetic nanoparticles have promising application photocatalytic reaction[44]. It is also worth to mention that the superparamagnetic $Fe_3O_4$ nanoparticles can be used as magnetic resonance imaging agent[45] and hyperthermia therapy agent[46].

# 1.2.3 Synthesis of magnetite nanoparticles

There are many synthetic procedures to synthesize magnetite particles for different applications such as co-precipitation[47], sonochemical[48], solvothermal[49], microemulsions[50] and metal-organic decomposition methods[51]. In this thesis, a metal-organic decomposition method has been used and

optimized based on the polyol and oleylamine route.

In the polyol route, different kinds of organometallic precursors for example metal actylacetonates ($M(acac)_3$) and metal carbonyls are used as the source of metal elements and short chain glycols such as ethylene glycol (EG), triethylene glycol (TREG) and benzyl alcohol are use as the reaction solvent to achieve the relative high reaction temperature (critical to get the highly crystalized structure) and as the functional capping ligand to stabilize the nanoparticles[52]. In some case some other organic molecules such as polyethylene glycol (PEG)[53], polyvinylpyrrolidone (PVP)[54] and chitosan[55] are also added into the mixture as the capping ligands for different applications[56]. Due to the presence of a capping ligand, the solubility of synthesized nanoparticles is excellent in polar solvents (e.g. water and ethanol).

In the oleylamine route, the reaction solvents are nonpolar, for example benzyl ether or oleylamine. In this procedure oleic acid and oleylamine are used as capping ligands to make the nanoparticles highly disperse in organic solvent such as hexane and cyclohexane[57, 58].

# 1.3 Ag nanoparticles

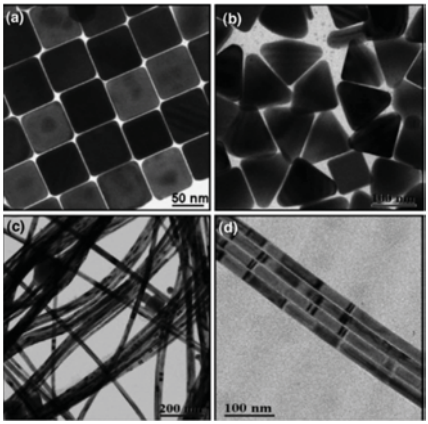


**Figure 1.4 TEM images of silver nanoparticles in different shape: (a) cubes; (b) triangles; (c) wires; (d) an alignment of nanowires[59].**

From ancient history until now, silver (Ag) has been widely used in currency, jewellery, and photography[21]. This metal has a face-centered cubic (fcc) crystal structure with only the single 5s electron is delocalized showing the highest electrical and thermal conductivity among all the metals and excellent optical properties, resulting in a widely application in electronic devices, thermal interfacial materials and conductors. For example, two-dimensional (2D) random networks of Ag nanowires have been proved to have potential application as transparent conductive films to replace the traditional rigid doped metal oxide conductive films (e.g. ITO) due to the fact that the low percolation threshold for Ag nanowires assures a high percentage of open areas in the conductive networks and the mechanical flexibility of Ag nanowires[60, 61].


**Figure 1.5 Example of the application of the Ag nanoparticles for 4-Nitrophenol Reduction[62]**

In recent years, due to its large surface-to-volume ratio and unique electronic structure, Ag nanoparticles have received tremendous attention because of its potential application as catalysts in many oxidation and oxidative coupling reactions such as massive production of formaldehyde from methanol[63]. It is also worth to mention that Ag nanoparticles are the only commercialized catalyst in available in the oxidation reaction of ethylene which is crucial for the production of industrial precursor[64].

Besides these applications mentioned above Ag nanoparticles also represent the application as a class of broad-spectrum antimicrobial reagents. For example, water filters with Ag nanoparticles and Ag nanowires are highly efficient in water cleaning industry[65, 66]. In addition, Ag nanoparticles also have applications in plasmonics research due to its strong surface plasmon resonances property coming from the strong coherent oscillation of free surface electrons[67, 68].

# 1.4 Carbon nanotubes

After the first report by Iijima in 1991[69], carbon nanotubes (CNTs), a vast of articles and books

have been dedicated to the unique and fantastic properties of carbon nanotubes. Generally speaking, CNTs can be defined as a tubular structure carbon material which was made entirely of rolling one or several layers of interconnected carbon atoms coaxially, with the diameter range from 1nm to tens of nanometer and the length up to micrometers or centimeters[70].

## 1.4.1 Classification of CNTs

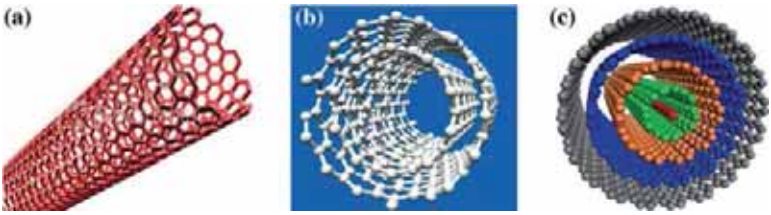


**Figure 1.6 Different types of CNTs a) single-walled carbon nanotubes (SWCNTs), b) double-walled carbon nanotubes (DWNTS) and c) multi-walled carbon nanotubes (MWCNTs)**

There are many ways to classify CNTs, first of all it is well known that carbon nanotubes can be classified into single-walled carbon nanotubes (SWCNTs, only one layer of carbon atoms), double-walled carbon nanotubes (DWNTS, two layers of carbon atoms) and multi-walled carbon nanotubes (MWCNTs, more than two layers of carbon atoms) according to the number of carbon atoms layers. The diameter of SWCNTs is from 0.7 nm from 1.2 nm while the diameter of MWCNTs is from 1.4 nm to 150 nm typically.

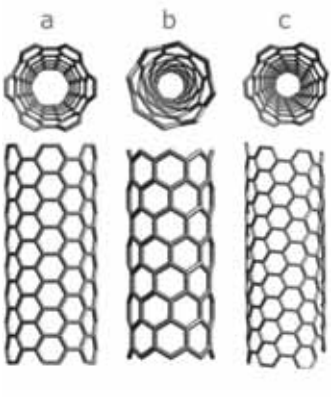


**Figure 1.7 Schematic model of (a) an armchair nanotube, (b) a zig-zag nanotube, and (c) a chiral nanotube**

According to their chiral indices ($n_1$, $n_2$), CNTs can be classified in zigzag[71], armchair[72] and chiral[73] structures. For armchair CNTs, the chiral indices $n_1$ and $n_2$ are equal while for zigzag CNTs, either $n_1$ or $n_2 = 0$. For other values of indices, CNTs are known as chiral CNTs. Depending upon their different structures, CNTs can exhibit metallic or semiconducting properties. By satisfying the condition $n_1$-$n_2$=3k (where k is an integer), the CNTs are always metallic, whereas satisfying the condition $n_1$-$n_2$ =3k±1 the CNTs are semiconducting in nature[74].

# 1.4.2 Properties of CNTs

Due to their small diameter and hollow geometry, CNTs always possess large specific surface area and high aspect ratio[75]. Some physical properties of CNTs are summarized in Table 1.2. The unique arrangement of carbon atoms gives the CNTs special electrical, thermal and mechanical properties; these properties will be discussed in the following paragraphs.

| Property | SWCNTs | MWCNTs |
|---|---|---|
| Specific gravity | 0.8g/cm$^3$ | <1.8g/cm$^3$ |
| Elastic modulus | 1.4TPa | 0.3-1TPa |
| Strength | 50-500GPa | 10-60GPa |
| Electric resistivity | 5-50μΩ•cm | |
| Thermal conductivity | 3000W/m/K | |
| Magnetic susceptibility | 22×106emu/g (perpendicular)<br>0.5×106emu/g (parallel) | |
| Thermal expansion | Negligible | |
| Thermal stability | 600-800°C in air and 2800°C in vacuum | |

**Table 1.2 Summary of physical properties of SWCNTs and MWCNTs[76].**

**Electrical properties**[77]: In general, the metallic CNTs can be considered as kind of highly conductive materials due to the unique structure of graphite and the quantum mechanical properties, which results in the near-total elimination of electron collisions (scattering). Therefore, the CNTs are ballistic conductors with their electrical resistance independent of the nanotube length. The CNTs can carry the highest current density compared with any other known material, with reported measurements as high as $10^9$A/cm$^2$, while copper wires have the current density around $10^6$A/cm$^2$ [78]. Like the discussion in the classification part, the CNTs can be classified into either metallic or semiconducting CNTs. The semiconducting SWCNTs may have excellent performance better in many applications involving charge transfer processes, for example bio-sensors, field emission devices, and photocatalytic application[79, 80]. In the meantime the metallic CNTs are preferred to be used as interconnect parts in electronic devices or as conductive filler in CNTs-composites[81].

**Thermal conductivity property**: Due to the strong in-plane C-C bonds, which provide the exceptional strength and stiffness against axial strains, the CNTs can exhibit high flexibility against non-axial strains and zero in-plane thermal expansions[82]. Theoretical studies predicted room temperature thermal conductivities of individual SWCNTs is up to 6600 W/(m*K)[83, 84]. Hence, CNTs could transmit nearly twice as much heat as isotopically pure diamond. Due to their high thermal conductivity and low in-plane expansion, CNTs show exciting applications in reinforcing additives in functional composite materials[85], electronics[86], bio-sensor and actuating devices[87].

**Mechanical Properties**: Because of the existence of strong C=C double bonds, CNTs have a very large Young's modulus in the axial direction (1.4TPa for SWCNTs)[88]. The elongation-to-failure of CNTs is about 20-30%, when their stiffness was taken into consideration, CNTs have a tensile strength well above 100 GPa which is the highest value as we known, while the tensile strength of steel is only about 1-2GPa[89, 90]. However, it is worth to mention that due to the presence of the defects (e.g. Stone-Wales defects) in the graphitic walls, relatively small values of both Young modulus and tensile strength are obtained in the experimental process. The excellent mechanical properties of CNTs combined with their high aspect ratio will make CNTs potentially suitable for applications in composite materials require anisotropic properties[91, 92].

In summary, the presence of these extraordinary properties of CNTs promises them exciting futures in variety of applications.

# 1.5 Carbon nanotubes composites synthesis and applications

With the variety of requirements coming from the industry and research field, many conventional materials, for example ceramic and metals, are not able to fulfil all the requirements for specific applications. The combination of two or even more kinds of materials could show better performance than their individual constituents, such as carbon nanofiber reinforced polymer composites[93, 94]. Because of their unique electrical, thermal and mechanical properties, CNTs are promising building blocks for hybrid materials[95].

The synthesis of CNTs hybrids materials can be described into two strategies, one is to connect the outer surface of CNTs with other components and another way is filling the CNTs with different materials. The synthetic procedures of decorating the outer surface of CNTs can be categorized as ex-situ and in-situ process.

## 1.5.1 Ex-situ approaches

As it has been described, ex-situ approaches can be divided into two steps, first nanoparticles or other components are synthesized in the desired morphology, then those materials are modified and attached to the surface of CNTs through electrostatic interaction, covalent or noncovalent bonds. In this method, the components and CNTs require modification with functional groups. The functional groups have an strong effect on the interaction between components and CNTs[95, 96].

**Covalent interactions:** In this method, the oxidation of CNTs results in a functionalisation with carboxyl groups on their surface which can be linked to other nanomaterials containing amine or mercapto groups on the surface. For example, MWCNTs first treated with a mixture of $H_2SO_4/HNO_3$ can be decorated with ZnS capped CdSe quantum dots containing amine groups ($QD\text{-}NH_2$)[97], Hydrophilic metal oxide nanoparticles like $Fe_3O_4$ and $TiO_2$ can be easily attached to the carboxylic functionalized CNTs[98, 99].

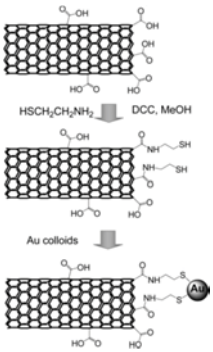


**Figure 1.8 Example of ex-situ process for the covalent attachment of Au nanoparticles to CNTs[100]**

**Noncovalent interactions:** Besides covalent interactions, nanomaterials can be attached on the surface of pristine CNTs through π-π stacking, Van der Waals interactions and hydrogen bonding. For instance, porphyrins[101, 102] and pyrene[103] organic compounds can attach to the pristine CNTs through π-π stacking interactions. Au nanoparticles decorated with a monolayer of octanethiols molecules tend to anchor on the CNTs surface in dichloromethane solution[104, 105] via hydrogen bonds and hydrophobic ineractions.

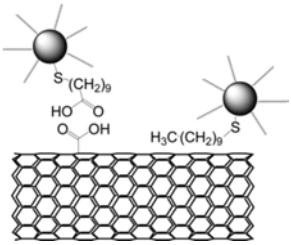


**Figure 1.9 Example of ex-situ process for the noncovalent attachment of Au nanoparticles to CNTs via hydrogen bonds and hydrophobic interactions[106]**

**Electrostatic interactions:** This approach uses the electrostatic force between modified CNTs and nanomaterials. The CNTs are first functionalized with ionic polyelectrolytes to be positively or negatively charged, for instance poly(diallyldimethylammonium chloride) (PDDA) will give a positively charged CNTs[107] and poly(sodium 4-styrenesulfonate) (PSS) will give a negatively charged CNTs[108]; then the CNTs will be covered with the nanomaterials containing the opposite electric charge. In this way metal and metal oxide nanoparticles could be strongly bond with the CNTs, for example positively charged $TiO_2$ nanoparticles could be immobilized on the SWCNTs[109].

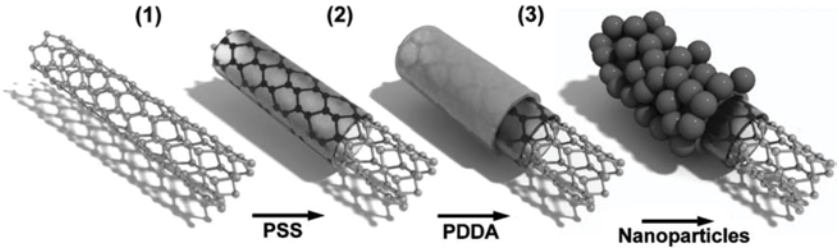


**Figure 1.10 Example of ex-situ process for the decoration of CNTs via electrostatic interactions using polyelectrolytes[110]**

In summary, the main advantage of ex-situ method is that the control of the nanomaterials attached

on the CNTs' surfaces which will give the CNTs hybrids desired properties for different applications. However, this approach needs chemically modifications of CNTs and nanomaterials in advance, which are often work-intensive.

## 1.5.2 In-situ process

The materials hybrid with CNTs can also be synthesized on the surface of CNTs, which is called in-situ approaches. The main advantage of this method is that the compound can be formed as a continuous film or coating with controlled thickness, or as disconnected units formed by nanoparticles and nanorods. In the meantime, the CNTs can act as template and support for synthesizing and stabilizing the nanomaterials.

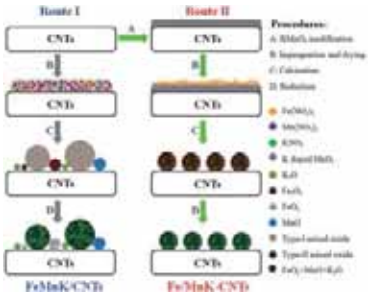


**Figure 1.11 Example of in-situ process for the decoration of CNTs with FeMnK nanoparticles through chemical reduction reaction[111]**

**Electrochemical Techniques:** As it is known, electrochemistry is a powerful tool for synthesizing different kind of nanoparticles. Metal and metal oxide nanoparticles can be prepared through the reduction or decomposition of metal complex, and the morphology of the obtained nanoparticles

and their distribution on the side wall of CNTs can be well manipulated via changing the reaction parameters. For instance, $SnO_2$ nanoparticles can be synthesized on the outside walls of CNTs for an efficient anode of Li-ion batteries[112], Silver nanoparticles can be formed on the vertically aligned MWCNTs for antibacterial applications[113].

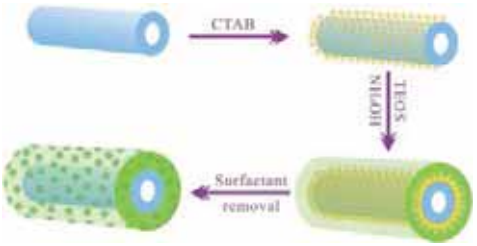


**Figure 1.12 Example of in-situ process for the coating of CNTs with mesoporous $SiO_2$ via sol-gel process[114]**

**Sol-gel process:** Due to the ability to produce ultrafine and uniform ceramic particles and thin-film coatings, sol-gel process is the most widely used method to synthesize CNTs nanocomposites. For example, $TiO_2$ and $SiO_2$ nanoparticles via the hydrolysis of (Titanium (IV) butoxide) TBOT and (Tetraethyl orthosilicate) TEOS for the applications in phototcatalysts, bio-imaging and drug delivery research[115-120].

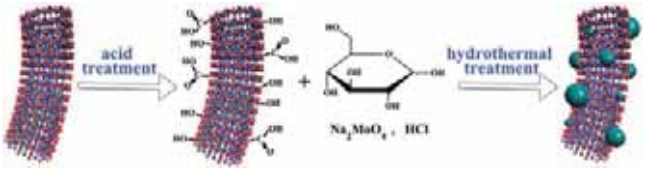


**Figure 1.13 Example of in-situ decoration of CNTs with $MoO_2$ nanoparticles via hydrothermal process[121]**

**Hydrothermal techniques:** The hydrothermal techniques would be able to form crystalline nanoparticles and films without further annealing and calcination treatments, this advantage has been utilized to synthesize CNTs nanocomposites decorated with crystalline nanowires and nanorods. For examples, $SnO_2$ and $MoO_2$ nanoparticles can be synthesized on the walls of CNTs for Li-ion battery anodes application[122, 123], ZnO nanoflowers and nanowires were prepared and combined with CNTs for the applications in photocatalysts and flexible supercapacitors and self-powered systems[124-126].

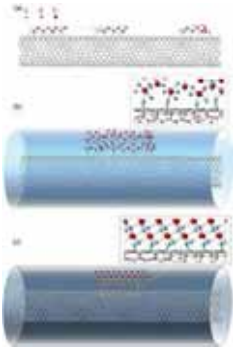

**Figure 1.14 Example of in-situ coating of CNTs with $TiO_2$ layer via ALD techniques[127]**

**Gas-phase deposition process:** Because of the excellent control of the size, shape and distribution of the obtained nanoparticles and films, the gas-phase deposition process has the possibility to synthesize CNTs nanocomposites with desired properties. For physical deposition, Platinum nanoparticles, ZnO films and $TiO_2$ films were uniformly deposited on the surface of CNTs via atomic layer deposition (ALD) for variety of applications[128-132]. On the other side, due to the high products purity, high deposition rate and easy to scale up, chemical vapor deposition processes are

also widely used to synthesize CNTs nanocomposites, such as $MnO_2$, $Fe_2O_3$ and $RuO_2$ nanoparticles were deposited on MNCNTs for electrochemical capacitors[133], ZnO thin film coated can be prepared via a water-assisted CVD process and used as an electron emitter[134].

Generally speaking, in the in-situ approach, the nanomaterials are directly formed on the surface of pristine or modified CNTs. The main advantages of this process are that the nanomaterials can be deposited as continuous amorphous or crystalline phase with well controlled morphology and properties and the variety of chemical and physical synthesis techniques can be used in the in-situ process.

# 1.5.3 Filling the CNTs

The tubular nature of CNTs allows the formation of hybrids materials via modification of the external walls or by encapsulation of selected materials into their cavity. In this way, the nanomaterials inside the CNTs can be protected from the oxidation/reaction resulted from the contact with the outside atmosphere. On the other side, nanomaterials, especially nanoparticles and nanowires can also be synthesized inside the CNTs; the confinement effect will yield nanomaterials with novel crystal structure, chemical composition and new properties. The first report about filling carbon nanostructure was a theoretical study by Pederson and Broughton who showed that fullerene tubules could draw molecules from liquid or vapor phase into their inner channels by capillary force and the earliest experiment report about filling CNTs toward filling CNTs with metal oxide particles (e.g. $Bi_2O_5$, PbO) and carbides (e.g. $Y_3C$, TiC)[135-137].

The CNTs can be filled during their synthesis, with the advantage of the encapsulated nanomaterials were completely protected by the CNTs and the CNTs integrity remains intact. But this process requires the encapsulated materials should be the catalysts for preparing CNTs (e.g. Ni, Co, Fe)[138]. On the other side the CNTs can also be filled after the synthesizing of CNTs. This approach is a multistep process; the CNTs should be treated to open the ends in the first step. And a post filling treatment was required for removing the excess nanomaterials through washing or vacuum annealing. The processes of filling CNTs mainly depend on the cavity diameter to be filled and on physical properties of the nanomaterials being immobilized inside the tubes such as solubility, melting point, surface tension, boiling point, viscosity, and decomposition temperature. These properties would further affect the size and the morphology of the inserted molecules nanomaterials and the filling efficiency resulting in the variety of the chemical and physical properties of the CNTs nanocomposites[139, 140].

Until now, a vast of organic and inorganic nanomaterials have been encapsulated or even been synthesized inside CNTs forming hybrid structures. For example, metallic nanowires[141], metal halides[142], fluorescent polystyrene beads[143], low dimensional silica-based materials[144], and individual layers of graphene[145] and related 2D materials[146] have all been encapsulated inside CNTs for the applications in biomedicine, catalysts and electronic device. Due to their small inner diameter, although single-walled carbon nanotubes and multi-walled carbon nanotubes with small diameters have filled with variety of nanomaterials, the obtained nanocomposites always lack bulk qualities and have low purity levels of synthesized nanomaterials inside the cavities. On another side, MWCNTs with relatively large diameter would be promising for encapsulating nanomaterials because of the relative large inner diameter[147]. Andrei N. Khlobystov and his colleagues

successfully assembled $Mn_3O_4$ nanoparticles inside MWCNTs[148] and synthesized Au nanoparticles inside MWCNTs[149, 150] making this kind of nanocomposites promising for the applications in catalysts and spintronic devices. Pt[151, 152] and $RuO_2$[153] nanoparticles can be synthesized inside the tubes showing potential applications in electrocatalysis, charge storage and fuel cell research. Organic compounds for example fullerene-tagged [Cu-(salen)] catalysts and fullerene-free Pd(II)-Salen catalysts were immobilized inside the tubes to form well-defined heterogeneous catalysts with excellent stability and recyclability[154, 155]. Recently, researchers also found out that Pt nanoparticles immobilized in shortened large diameter MWCNTs could form an extremely stable electrocatalysts shown superior properties compared with commercial Pt/C electrocatalyst[156]. It is also worth to mention that MWCNTs loaded with magnetic nanoparticles exhibit a large variety of current and potential applications in hyperthermia therapeutic and magnetic resonance imaging research[157].

## 1.5.4 Applications of CNTs nanocomposites

Due to the extraordinary properties of CNTs and the combination of the advantages from the nanomaterials immobilized on the surface or in the cavity of the CNTs, CNTs nanocomposites shown exciting prospects and variety of applications in catalysts, sensors, supercapacitors and biomedicine research.

In the research about photocatalytic reactions and photovoltaic, CNTs decorated with metal and oxide nanoparticles are considered as the promising candidates to increasing the efficiency. For example, $TiO_2$ nanoparticles can be attached to the surface of CNTs to obtain new kind of

phototcatalysts for hydrogen production reaction with large enhancements of efficiency[158-160]. On the other side light-harvesting semiconductor nanoparticles and metal oxide nanoparticles, for example $TiO_2$ NPs, CdS, CdTe or CdSe QDs, can be supported on the CNTs, due to the excellent property of electron transferring, the CNTs/QDs nanocomposites are very attractive for their contribution to the photoconversion efficiency in the solar cell application[161-166].

In contrast with the traditional metal oxide sensors, CNTs have extremely high adsorption index due to their large specific surface area resulting the plenty of active sites[167-170]. For instance, 9,9-dioctylfluorene derivatives conjugated with SWCNTs demonstrated that the whole nanocomposites have high sensitivity as the nitrogen dioxide gas sensors[171]. $Co_3O_4$ nanoparticles can be immobilized on the surface of CNTs forming a heterostructured nanocomposites that exhibited promising application in CO gas detection at room temperature[172]. Chitosan decorated CNTs covalent immobilized on Au electrodes were used as an amperometric glucose biosensors showing a good linear response to glucose in the concentration of glucose and high sensitivity[173, 174].

Due to the exceptional electronic properties, CNTs could allow ballistic transport of electrons, because of that, CNTs are considered as a promising material for supercapacitors. After the decorating of the electroactive nanomaterials, CNTs nanocomposites showed enhancements of capacitance values[175-177]. For example, $NiCo_2S_4$ and nitrogen-doped porous carbon monoliths can be combined with CNTs to form high performance supercapacitors with good pseudocapacitance properties[178, 179]. Additionally, ZnO QDs, $MnO_2$, $Co_3O_4$ and Ni–Co–S nanosheets can also be attached to the surface of CNTs to obtain supercapacitor devices with flexible, stretchable and

compressible mechanical properties[180-184].

Finally, CNTs combined with many biomolecules, metal and metal oxide nanoparticles, metal organic compounds also have exciting applications in biomedicine research. Mesoporous silica coated SWCNTs can be used as a multifunctional light-responsive platform for cancer therapy[185]. Gadolinium chelate molecules were decorated on the MWCNTs through covalent interactions, the obtained nanocomposites showed high efficiency in $T_1$-weighted magnetic resonance imaging application[186]. CNTs filled or decorated with $Fe_3O_4$ nanoparticles, radioactively metals, radionuclide compounds exhibited attractive prospect in bio-imaging, target therapy, diagnose and drug delivery applications[187-191].

For all of these applications and more, research work about improving the properties of CNTs nanocomposites are being carried out. Considering the outstanding results in recent preliminary studies, we believe the CNTs nanocomposites would have the promising potential applications in many research fields and do great contribution to our society.

# 1.6 Objectives of thesis

This doctoral research has been carried out in the “inorganic nanoparticles and functional ligands” group. Based on the well-developed synthetic routes about nanoparticles preparation and research results about metal and metal oxide nanoparticles in this group, the major research field of this thesis focus on magnetic nanoparticles nanocomposites with complex structures. On the one hand, the nanomaterials will be prepared, as well as fully characterized with modern analytical

techniques. On the other hand, this thesis also seeks to find potential applications for those nanomaterials in different areas such as catalysts and biomedicine.

The details of objectives of the thesis are presented in the following paragraphs.

1 Synthesis of $Fe_3O_4$@$SiO_2$ core-shell nanoparticles through normal reverse microemulsion and microwave assistance reverse microemulsion method. Study the effects of the reaction parameters on the final core-shell nanoparticles. The main purpose is to establish an optimized synthetic procedure for preparation of $Fe_3O_4$@$SiO_2$ core-shell nanoparticles.

2 Synthesis of $Fe_3O_4$ nanoparticles inside CNTs via normal and microwave irradiated solvent thermal methods. The obtained CNTs nanocomposites will be further coated with $SiO_2$ layer to protect the inner nanoparticles to form nanocapsules.

3 The MRI imaging propertes of the $Fe_3O_4$@$SiO_2$ core-shell nanoparticles and $Fe_3O_4$@CNTs nanocomposites will be studied for their potential application in bio-imaging research.

4 Functionalization of $Fe_3O_4$@$SiO_2$ core-shell nanoparticles to be used in different chemical reactions as catalyst.

5 The cytotoxicity of synthesized $Fe_3O_4$@$SiO_2$ core-shell nanoparticles will be investigated. The obtained $Fe_3O_4$@$SiO_2$ core-shell nanoparticles will be decorated with different biomolecules. The final goal of this work is to study their potential application in bio-medicine research. Such as bio-sensors, hyperthermia therapy and magnetic manipulation of cancer cells.

# References


1. L.-S. Zhong, J.-S. Hu, A.-M. Cao, Q. Liu, W.-G. Song and L.-J. Wan, *Chemistry of Materials*, 2007, **19**, 1648-1655.
2. A. F. Khan, D. A. C. Brownson, E. P. Randviir, G. C. Smith and C. E. Banks, *Analytical Chemistry*, 2016, **88**, 9729-9737.
3. Y. Liu, J. F. Flores and J. Q. Lu, *The Journal of Physical Chemistry C*, 2014, **118**, 19387-19395.
4. G. Yi, Y. Peng and Z. Gao, *Chemistry of Materials*, 2011, **23**, 2729-2734.
5. Y. Peng, H.-Y. Zhou and Z.-H. Wang, *CrystEngComm*, 2012, **14**, 2812-2816.
6. P. Liu, Q. Hao, X. Xia, L. Lu, W. Lei and X. Wang, *The Journal of Physical Chemistry C*, 2015, **119**, 8537-8546.
7. S. Xu, Z. Yan, K.-I. Jang, W. Huang, H. Fu, J. Kim, Z. Wei, M. Flavin, J. McCracken, R. Wang, A. Badea, Y. Liu, D. Xiao, G. Zhou, J. Lee, H. U. Chung, H. Cheng, W. Ren, A. Banks, X. Li, U. Paik, R. G. Nuzzo, Y. Huang, Y. Zhang and J. A. Rogers, *Science*, 2015, **347**, 154-159.
8. K. Aoki, H. T. Miyazaki, H. Hirayama, K. Inoshita, T. Baba, K. Sakoda, N. Shinya and Y. Aoyagi, *Nat Mater*, 2003, **2**, 117-121.
9. D. Fattakhova-Rohlfing, A. Zaleska and T. Bein, *Chemical Reviews*, 2014, **114**, 9487-9558.
10. T. Zhu, L. Zhu, J. Wang and G. W. Ho, *Journal of Materials Chemistry A*, 2016, **4**, 13916-13922.
11. X. Peng, L. Peng, C. Wu and Y. Xie, *Chemical Society Reviews*, 2014, **43**, 3303-3323.
12. Y. Guo, K. Xu, C. Wu, J. Zhao and Y. Xie, *Chemical Society Reviews*, 2015, **44**, 637-646.
13. *Journal of Materials Chemistry*, 2009, **19**, 826-827.
14. J. Yuan, Y. Xu and A. H. E. Muller, *Chemical Society Reviews*, 2011, **40**, 640-655.
15. R. K. Joshi and J. J. Schneider, *Chemical Society Reviews*, 2012, **41**, 5285-5312.
16. C. Zhang, Y. Yan, Y. Sheng Zhao and J. Yao, *Annual Reports Section "C" (Physical Chemistry)*, 2013, **109**, 211-239.

17. Z. Yu, L. Tetard, L. Zhai and J. Thomas, *Energy & Environmental Science*, 2015, **8**, 702-730.
18. P. Russo, R. Liang, E. Jabari, E. Marzbanrad, E. Toyserkani and Y. N. Zhou, *Nanoscale*, 2016, **8**, 8863-8877.
19. X. Gong, Y. Bao, C. Qiu and C. Jiang, *Chemical Communications*, 2012, **48**, 7003-7018.
20. L. M. Liz-Marzán, *Materials Today*, 2004, **7**, 26-31.
21. Y. Xia, Y. Xiong, B. Lim and S. E. Skrabalak, *Angewandte Chemie International Edition*, 2009, **48**, 60-103.
22. J. Kruenate, R. Tongpool, T. Panyathanmaporn and P. Kongrat, *Surface and Interface Analysis*, 2004, **36**, 1044-1047.
23. Y. Wang, G. Wang, Y. Xiao, Y. Yang and R. Tang, *ACS Applied Materials & Interfaces*, 2014, **6**, 19092-19099.
24. E. Berardo and M. A. Zwijnenburg, *The Journal of Physical Chemistry C*, 2015, **119**, 13384-13393.
25. J. M. Pietryga, Y.-S. Park, J. Lim, A. F. Fidler, W. K. Bae, S. Brovelli and V. I. Klimov, *Chemical Reviews*, 2016, **116**, 10513-10622.
26. G. Xu, S. Zeng, B. Zhang, M. T. Swihart, K.-T. Yong and P. N. Prasad, *Chemical Reviews*, 2016, **116**, 12234-12327.
27. K. A. S. Fernando, S. Sahu, Y. Liu, W. K. Lewis, E. A. Guliants, A. Jafariyan, P. Wang, C. E. Bunker and Y.-P. Sun, *ACS Applied Materials & Interfaces*, 2015, **7**, 8363-8376.
28. N. Hildebrandt, *ACS Nano*, 2011, **5**, 5286-5290.
29. R. Narayanan and M. A. El-Sayed, *The Journal of Physical Chemistry B*, 2005, **109**, 12663-12676.
30. B. J. Wiley, Z. Wang, J. Wei, Y. Yin, D. H. Cobden and Y. Xia, *Nano Letters*, 2006, **6**, 2273-2278.
31. L. Yonghua, Z. Yaohua, L. Tong, S. Masaaki and L. Xingguo, *Nanotechnology*, 2006, **17**, 1797.
32. J. Y. T. Chong, X. Mulet, D. J. Keddie, L. Waddington, S. T. Mudie, B. J. Boyd and C. J. Drummond, *Langmuir*, 2015, **31**, 2615-2629.
33. P. Pramod, S. T. S. Joseph and K. G. Thomas, *Journal of the American Chemical Society*,

2007, **129**, 6712-6713.

34. P. E. Dumas and A. Zozulin, *Journal of Chemical Education*, 1974, **51**, 784.
35. D. L. Leslie-Pelecky and R. D. Rieke, *Chemistry of Materials*, 1996, **8**, 1770-1783.
36. J. Tuček, R. Zbořil, A. Namai and S.-i. Ohkoshi, *Chemistry of Materials*, 2010, **22**, 6483-6505.
37. K. R. S. P. Meher, C. Martin, V. Caignaert, F. Damay and A. Maignan, *Chemistry of Materials*, 2014, **26**, 830-836.
38. K. Deshpande, M. Nersesyan, A. Mukasyan and A. Varma, *Industrial & Engineering Chemistry Research*, 2005, **44**, 6196-6199.
39. M. Mahmoudi, H. Hofmann, B. Rothen-Rutishauser and A. Petri-Fink, *Chemical Reviews*, 2012, **112**, 2323-2338.
40. Magnetic Materials Background Information, http://www.birmingham.ac.uk/research/activity/metallurgy-materials/magnets/Magnetic-Materials-Background-Information.aspx, (accessed Janurary 2017)
41. N. Lee, D. Yoo, D. Ling, M. H. Cho, T. Hyeon and J. Cheon, *Chemical Reviews*, 2015, **115**, 10637-10689.
42. J. Wang, X. Wu, C. Wang, Z. Rong, H. Ding, H. Li, S. Li, N. Shao, P. Dong, R. Xiao and S. Wang, *ACS Applied Materials & Interfaces*, 2016, **8**, 19958-19967.
43. J. Zhang, M. C. Shin, A. E. David, J. Zhou, K. Lee, H. He and V. C. Yang, *Molecular Pharmaceutics*, 2013, **10**, 3892-3902.
44. K.-H. Choi, K.-K. Wang, E. P. Shin, S.-L. Oh, J.-S. Jung, H.-K. Kim and Y.-R. Kim, *The Journal of Physical Chemistry C*, 2011, **115**, 3212-3219.
45. V. Patsula, L. Kosinová, M. Lovrić, L. Ferhatovic Hamzić, M. Rabyk, R. Konefal, A. Paruzel, M. Šlouf, V. Herynek, S. Gajović and D. Horák, *ACS Applied Materials & Interfaces*, 2016, **8**, 7238-7247.
46. Y. V. Kolen'ko, M. Bañobre-López, C. Rodríguez-Abreu, E. Carbó-Argibay, A. Sailsman, Y. Piñeiro-Redondo, M. F. Cerqueira, D. Y. Petrovykh, K. Kovnir, O. I. Lebedev and J. Rivas, *The Journal of Physical Chemistry C*, 2014, **118**, 8691-8701.
47. F. Vereda, J. de Vicente and R. Hidalgo-Álvarez, *Langmuir*, 2007, **23**, 3581-3589.

48. M. Abbas, S. R. Torati and C. Kim, *Nanoscale*, 2015, **7**, 12192-12204.
49. F. B. F. Silva, E. C. Paris, G. M. da Costa and C. Ribeiro, *RSC Advances*, 2014, **4**, 53265-53272.
50. J. Baier, J. Koetz, S. Kosmella, B. Tiersch and H. Rehage, *The Journal of Physical Chemistry B*, 2007, **111**, 8612-8618.
51. B. Wang, B. Wang, P. Wei, X. Wang and W. Lou, *Dalton Transactions*, 2012, **41**, 896-899.
52. E. Solano, L. Perez-Mirabet, F. Martinez-Julian, R. Guzmán, J. Arbiol, T. Puig, X. Obradors, R. Yañez, A. Pomar, S. Ricart and J. Ros, *Journal of Nanoparticle Research*, 2012, **14**, 1034.
53. M. Mahmoudi, A. Simchi, M. Imani and U. O. Häfeli, *The Journal of Physical Chemistry C*, 2009, **113**, 8124-8131.
54. X. Lu, M. Niu, R. Qiao and M. Gao, *The Journal of Physical Chemistry B*, 2008, **112**, 14390-14394.
55. A. Konwar, S. Kalita, J. Kotoky and D. Chowdhury, *ACS Applied Materials & Interfaces*, 2016, **8**, 20625-20634.
56. L. H. Reddy, J. L. Arias, J. Nicolas and P. Couvreur, *Chemical Reviews*, 2012, **112**, 5818-5878.
57. L. Pérez-Mirabet, E. Solano, F. Martínez-Julián, R. Guzmán, J. Arbiol, T. Puig, X. Obradors, A. Pomar, R. Yáñez, J. Ros and S. Ricart, *Materials Research Bulletin*, 2013, **48**, 966-972.
58. C. Y. Lu, T. Puig, X. Obradors, S. Ricart and J. Ros, *RSC Advances*, 2016, **6**, 88762-88769.
59. V. K. Sharma, R. A. Yngard and Y. Lin, *Advances in Colloid and Interface Science*, 2009, **145**, 83-96.
60. M. Singh, T. R. Rana, S. Kim, K. Kim, J. H. Yun and J. Kim, *ACS Applied Materials & Interfaces*, 2016, **8**, 12764-12771.
61. D. S. Ghosh, T. L. Chen, V. Mkhitaryan and V. Pruneri, *ACS Applied Materials & Interfaces*, 2014, **6**, 20943-20948.
62. B. Baruah, G. J. Gabriel, M. J. Akbashev and M. E. Booher, *Langmuir*, 2013, **29**, 4225-4234.
63. C. Han, X. Yang, G. Gao, J. Wang, H. Lu, J. Liu, M. Tong and X. Liang, *Green Chemistry*, 2014, **16**, 3603-3615.
64. J. Zhao, M. R. Madachik, K. M. O'Donnell, G. Moore, L. Thomsen, O. Warschkow, S. R.

Schofield and A. Teplyakov, *The Journal of Physical Chemistry C*, 2016, **120**, 28672-28681.

65. D. M. Eby, H. R. Luckarift and G. R. Johnson, *ACS Applied Materials & Interfaces*, 2009, **1**, 1553-1560.
66. A. Francesko, L. Blandón, M. Vázquez, P. Petkova, J. Morató, A. Pfeifer, T. Heinze, E. Mendoza and T. Tzanov, *ACS Applied Materials & Interfaces*, 2015, **7**, 9792-9799.
67. W. J. Cho, Y. Kim and J. K. Kim, *ACS Nano*, 2012, **6**, 249-255.
68. S. K. Bhunia, L. Zeiri, J. Manna, S. Nandi and R. Jelinek, *ACS Applied Materials & Interfaces*, 2016, **8**, 25637-25643.
69. S. Iijima, *Nature*, 1991, **354**, 56-58.
70. S. Iijima and T. Ichihashi, *Nature*, 1993, **363**, 603-605.
71. C. Blum, N. Stürzl, F. Hennrich, S. Lebedkin, S. Heeg, H. Dumlich, S. Reich and M. M. Kappes, *ACS Nano*, 2011, **5**, 2847-2854.
72. E. H. Hároz, W. D. Rice, B. Y. Lu, S. Ghosh, R. H. Hauge, R. B. Weisman, S. K. Doorn and J. Kono, *ACS Nano*, 2010, **4**, 1955-1962.
73. Y. Sato, K. Yanagi, Y. Miyata, K. Suenaga, H. Kataura and S. Iijima, *Nano Letters*, 2008, **8**, 3151-3154.
74. B. K. Kaushik and M. K. Majumder, in *Carbon Nanotube Based VLSI Interconnects: Analysis and Design*, Springer India, New Delhi, 2015, pp. 17-37.
75. A. N. Khlobystov, *ACS Nano*, 2011, **5**, 9306-9312.
76. O. M. Yaghi, G. Li and H. Li, *Nature*, 1995, **378**, 703-706.
77. J. Opatkiewicz, M. C. LeMieux and Z. Bao, *ACS Nano*, 2010, **4**, 2975-2978.
78. C. N. R. Rao and A. K. Cheetham, *Journal of Materials Chemistry*, 2001, **11**, 2887-2894.
79. K. Yanagi, H. Udoguchi, S. Sagitani, Y. Oshima, T. Takenobu, H. Kataura, T. Ishida, K. Matsuda and Y. Maniwa, *ACS Nano*, 2010, **4**, 4027-4032.
80. T. Tanaka, H. Jin, Y. Miyata, S. Fujii, H. Suga, Y. Naitoh, T. Minari, T. Miyadera, K. Tsukagoshi and H. Kataura, *Nano Letters*, 2009, **9**, 1497-1500.
81. D. Dutta, R. M. Sankaran and V. R. Bhethanabotla, *Chemistry of Materials*, 2014, **26**, 4943-4950.
82. C. Wei, D. Srivastava and K. Cho, *Nano Letters*, 2002, **2**, 647-650.

83. C. Ren, W. Zhang, Z. Xu, Z. Zhu and P. Huai, *The Journal of Physical Chemistry C*, 2010, **114**, 5786-5791.
84. S. Berber, Y.-K. Kwon and D. Tománek, *Physical Review Letters*, 2000, **84**, 4613-4616.
85. Y. Pan, H. Bao and L. Li, *ACS Applied Materials & Interfaces*, 2011, **3**, 4819-4830.
86. R. Martel, *ACS Nano*, 2008, **2**, 2195-2199.
87. O. N. Oliveira, R. M. Iost, J. R. Siqueira, F. N. Crespilho and L. Caseli, *ACS Applied Materials & Interfaces*, 2014, **6**, 14745-14766.
88. B. Lukić, J. W. Seo, R. R. Bacsa, S. Delpeux, F. Béguin, G. Bister, A. Fonseca, J. B. Nagy, A. Kis, S. Jeney, A. J. Kulik and L. Forró, *Nano Letters*, 2005, **5**, 2074-2077.
89. M.-F. Yu, B. S. Files, S. Arepalli and R. S. Ruoff, *Physical Review Letters*, 2000, **84**, 5552-5555.
90. S. G. Miller, T. S. Williams, J. S. Baker, F. Solá, M. Lebron-Colon, L. S. McCorkle, N. G. Wilmoth, J. Gaier, M. Chen and M. A. Meador, *ACS Applied Materials & Interfaces*, 2014, **6**, 6120-6126.
91. S. Hong, T. Lundstrom, R. Ghosh, H. Abdi, J. Hao, S. K. Jeoung, P. Su, J. Suhr, A. Vaziri, N. Jalili and Y. J. Jung, *ACS Applied Materials & Interfaces*, 2016, **8**, 34061-34067.
92. Q. Li, C. Liu, Y.-H. Lin, L. Liu, K. Jiang and S. Fan, *ACS Nano*, 2015, **9**, 409-418.
93. L. Ci, J. Suhr, V. Pushparaj, X. Zhang and P. M. Ajayan, *Nano Letters*, 2008, **8**, 2762-2766.
94. B. Gao, R. Zhang, F. Gao, M. He, C. Wang, L. Liu, L. Zhao and H. Cui, *Langmuir*, 2016, **32**, 8339-8349.
95. L. Dai, D. W. Chang, J.-B. Baek and W. Lu, *Small*, 2012, **8**, 1130-1166.
96. M. Batmunkh, M. J. Biggs and J. G. Shapter, *Small*, 2015, **11**, 2963-2989.
97. S. Ravindran, S. Chaudhary, B. Colburn, M. Ozkan and C. S. Ozkan, *Nano Letters*, 2003, **3**, 447-453.
98. Y. Yang, J. Li, D. Chen and J. Zhao, *ACS Applied Materials & Interfaces*, 2016, **8**, 26730-26739.
99. Y. Yao, G. Li, S. Ciston, R. M. Lueptow and K. A. Gray, *Environmental Science & Technology*, 2008, **42**, 4952-4957.
100. J. Chen, M. A. Hamon, H. Hu, Y. Chen, A. M. Rao, P. C. Eklund and R. C. Haddon, *Science*,

1998, **282**, 95-98.

101. A. Satake, Y. Miyajima and Y. Kobuke, *Chemistry of Materials*, 2005, **17**, 716-724.
102. H. Ozawa, X. Yi, T. Fujigaya, Y. Niidome, T. Asano and N. Nakashima, *Journal of the American Chemical Society*, 2011, **133**, 14771-14777.
103. M. Li, P. Xu, J. Yang, H. Ying, K. Haubner, L. Dunsch and S. Yang, *The Journal of Physical Chemistry C*, 2011, **115**, 4584-4593.
104. A. V. Ellis, K. Vijayamohanan, R. Goswami, N. Chakrapani, L. S. Ramanathan, P. M. Ajayan and G. Ramanath, *Nano Letters*, 2003, **3**, 279-282.
105. S. Bhattacharya and S. K. Samanta, *Chemical Reviews*, 2016, **116**, 11967-12028.
106. L. Han, W. Wu, F. L. Kirk, J. Luo, M. M. Maye, N. N. Kariuki, Y. Lin, C. Wang and C.-J. Zhong, *Langmuir*, 2004, **20**, 6019-6025.
107. S. Wang, D. Yu and L. Dai, *Journal of the American Chemical Society*, 2011, **133**, 5182-5185.
108. X. Hu, L. Chen, Y. Zhang, Q. Hu, J. Yang and Y. Chen, *Chemistry of Materials*, 2014, **26**, 6293-6302.
109. J. Sun, M. Iwasa, L. Gao and Q. Zhang, *Carbon*, 2004, **42**, 895-899.
110. M. A. Correa-Duarte and L. M. Liz-Marzan, *Journal of Materials Chemistry*, 2006, **16**, 22-25.
111. D. Wang, X. Zhou, J. Ji, X. Duan, G. Qian, X. Zhou, D. Chen and W. Yuan, *Journal of Materials Chemistry A*, 2015, **3**, 4560-4567.
112. X. Liu, M. Wu, M. Li, X. Pan, J. Chen and X. Bao, *Journal of Materials Chemistry A*, 2013, **1**, 9527-9535.
113. O. Akhavan, M. Abdolahad, Y. Abdi and S. Mohajerzadeh, *Journal of Materials Chemistry*, 2011, **21**, 387-393.
114. M. Zhang, Y. Wu, X. Feng, X. He, L. Chen and Y. Zhang, *Journal of Materials Chemistry*, 2010, **20**, 5835-5842.
115. M.-Q. Yang, N. Zhang and Y.-J. Xu, *ACS Applied Materials & Interfaces*, 2013, **5**, 1156-1164.
116. S. Sadhu and P. Poddar, *The Journal of Physical Chemistry C*, 2014, **118**, 19363-19373.
117. S. Zhang, H. Niu, Y. Lan, C. Cheng, J. Xu and X. Wang, *The Journal of Physical Chemistry C*, 2011, **115**, 22025-22034.

118. R. K. Singh, K. D. Patel, J.-J. Kim, T.-H. Kim, J.-H. Kim, U. S. Shin, E.-J. Lee, J. C. Knowles and H.-W. Kim, *ACS Applied Materials & Interfaces*, 2014, **6**, 2201-2208.

119. L. Zhang, W. C. Geng, S. Z. Qiao, H. J. Zheng, G. Q. Lu and Z. F. Yan, *ACS Applied Materials & Interfaces*, 2010, **2**, 2767-2772.

120. Z. Sun, H. Zhang, Y. Zhao, C. Huang, R. Tao, Z. Liu and Z. Wu, *Langmuir*, 2011, **27**, 6244-6251.

121. S. Qiu, G. Lu, J. Liu, H. Lyu, C. Hu, B. Li, X. Yan, J. Guo and Z. Guo, *RSC Advances*, 2015, **5**, 87286-87294.

122. R.-M. Kong, N.-N. Sun, F. Qu, H. Wu, H. Wang and J. You, *RSC Advances*, 2015, **5**, 86849-86854.

123. Y.-H. Jin, K.-M. Min, S.-D. Seo, H.-W. Shim and D.-W. Kim, *The Journal of Physical Chemistry C*, 2011, **115**, 22062-22067.

124. R. Zhang, L. Fan, Y. Fang and S. Yang, *Journal of Materials Chemistry*, 2008, **18**, 4964-4970.

125. W.-D. Zhang, L.-C. Jiang and J.-S. Ye, *The Journal of Physical Chemistry C*, 2009, **113**, 16247-16253.

126. P. Yang, X. Xiao, Y. Li, Y. Ding, P. Qiang, X. Tan, W. Mai, Z. Lin, W. Wu, T. Li, H. Jin, P. Liu, J. Zhou, C. P. Wong and Z. L. Wang, *ACS Nano*, 2013, **7**, 2617-2626.

127. Y. Zhang, C. Guerra-Nuñez, M. Li, J. Michler, H. G. Park, M. D. Rossell, R. Erni and I. Utke, *Chemistry of Materials*, 2016, **28**, 3488-3496.

128. R. M. Silva, M. C. Ferro, J. R. Araujo, C. A. Achete, G. Clavel, R. F. Silva and N. Pinna, *Langmuir*, 2016, **32**, 7038-7044.

129. C.-T. Hsieh, Y.-Y. Liu, D.-Y. Tzou and W.-Y. Chen, *The Journal of Physical Chemistry C*, 2012, **116**, 26735-26743.

130. H.-C. Wen, C.-I. Hung, H.-J. Tsai, C.-K. Lu, Y.-C. Lai and W.-K. Hsu, *Journal of Materials Chemistry*, 2012, **22**, 13747-13750.

131. C. Guerra-Nunez, Y. Zhang, M. Li, V. Chawla, R. Erni, J. Michler, H. G. Park and I. Utke, *Nanoscale*, 2015, **7**, 10622-10633.

132. M. Xie, X. Sun, H. Sun, T. Porcelli, S. M. George, Y. Zhou and J. Lian, *Journal of Materials Chemistry A*, 2016, **4**, 537-544.

133. M. B. Sassin, C. N. Chervin, D. R. Rolison and J. W. Long, *Accounts of Chemical Research*, 2013, **46**, 1062-1074.

134. J. Liu, X. Li and L. Dai, *Advanced Materials*, 2006, **18**, 1740-1744.

135. P. M. Ajayan and S. Iijima, *Nature*, 1993, **361**, 333-334.

136. P. M. Ajayan, T. W. Ebbesen, T. Ichihashi, S. Iijima, K. Tanigaki and H. Hiura, *Nature*, 1993, **362**, 522-525.

137. S. Seraphin, D. Zhou, J. Jiao, J. C. Withers and R. Loutfy, *Nature*, 1993, **362**, 503-503.

138. A. Huczko, H. Lange and T. Sogabe, *The Journal of Physical Chemistry A*, 2000, **104**, 10708-10712.

139. B. W. Smith, M. Monthioux and D. E. Luzzi, *Nature*, 1998, **396**, 323-324.

140. M. Monthioux, E. Flahaut and J. P. Cleuziou, *Journal of Materials Research*, 2006, **21**, 2774-2793.

141. L. Guan, K. Suenaga, S. Okubo, T. Okazaki and S. Iijima, *Journal of the American Chemical Society*, 2008, **130**, 2162-2163.

142. J. Sloan, A. I. Kirkland, J. L. Hutchison and M. L. H. Green, *Chemical Communications*, 2002, 1319-1332.

143. B. M. Kim, S. Qian and H. H. Bau, *Nano Letters*, 2005, **5**, 873-878.

144. Z. Liu, S.-K. Joung, T. Okazaki, K. Suenaga, Y. Hagiwara, T. Ohsuna, K. Kuroda and S. Iijima, *ACS Nano*, 2009, **3**, 1160-1166.

145. A. Chuvilin, E. Bichoutskaia, M. C. Gimenez-Lopez, T. W. Chamberlain, G. A. Rance, N. Kuganathan, J. Biskupek, U. Kaiser and A. N. Khlobystov, *Nat Mater*, 2011, **10**, 687-692.

146. L. Cabana, B. Ballesteros, E. Batista, C. Magén, R. Arenal, J. Oró-Solé, R. Rurali and G. Tobias, *Advanced Materials*, 2014, **26**, 2016-2021.

147. E. Castillejos, P.-J. Debouttière, L. Roiban, A. Solhy, V. Martinez, Y. Kihn, O. Ersen, K. Philippot, B. Chaudret and P. Serp, *Angewandte Chemie*, 2009, **121**, 2567-2571.

148. M. d. C. Gimenez-Lopez, A. La Torre, M. W. Fay, P. D. Brown and A. N. Khlobystov, *Angewandte Chemie International Edition*, 2013, **52**, 2051-2054.

149. A. La Torre, G. A. Rance, J. El Harfi, J. Li, D. J. Irvine, P. D. Brown and A. N. Khlobystov, *Nanoscale*, 2010, **2**, 1006-1010.

150. A. La Torre, M. d. C. Giménez-López, M. W. Fay, G. A. Rance, W. A. Solomonsz, T. W. Chamberlain, P. D. Brown and A. N. Khlobystov, *ACS Nano*, 2012, **6**, 2000-2007.

151. G. Zhao, J. He, C. Zhang, J. Zhou, X. Chen and T. Wang, *The Journal of Physical Chemistry C*, 2008, **112**, 1028-1033.

152. B. Cornelio, A. R. Saunders, W. A. Solomonsz, M. Laronze-Cochard, A. Fontana, J. Sapi, A. N. Khlobystov and G. A. Rance, *Journal of Materials Chemistry A*, 2015, **3**, 3918-3927.

153. R. Vellacheri, V. K. Pillai and S. Kurungot, *Nanoscale*, 2012, **4**, 890-896.

154. M. A. Lebedeva, T. W. Chamberlain, M. Schröder and A. N. Khlobystov, *Chemistry of Materials*, 2014, **26**, 6461-6466.

155. M. A. Lebedeva, T. W. Chamberlain, A. Thomas, B. E. Thomas, C. T. Stoppiello, E. Volkova, M. Suyetin and A. N. Khlobystov, *Nanoscale*, 2016, **8**, 11727-11737.

156. M. del Carmen Gimenez-Lopez, A. Kurtoglu, D. A. Walsh and A. N. Khlobystov, *Advanced Materials*, 2016, **28**, 9103-9108.

157. A. Stopin, F. Pineux, R. Marega and D. Bonifazi, *Chemistry – A European Journal*, 2015, **21**, 9288-9301.

158. K.-J. Chao, W.-Y. Cheng, T.-H. Yu and S.-Y. Lu, *Carbon*, 2013, **62**, 69-75.

159. Y. Yan, J. Miao, Z. Yang, F.-X. Xiao, H. B. Yang, B. Liu and Y. Yang, *Chemical Society Reviews*, 2015, **44**, 3295-3346.

160. J. Park and W. Choi, *The Journal of Physical Chemistry C*, 2009, **113**, 20974-20979.

161. J. Wang, Y. Lin, M. Pinault, A. Filoramo, M. Fabert, B. Ratier, J. Bouclé and N. Herlin-Boime, *ACS Applied Materials & Interfaces*, 2015, **7**, 51-56.

162. K. E. Tettey, M. Q. Yee and D. Lee, *ACS Applied Materials & Interfaces*, 2010, **2**, 2646-2652.

163. L. Wang, H. Liu, R. M. Konik, J. A. Misewich and S. S. Wong, *Chemical Society Reviews*, 2013, **42**, 8134-8156.

164. Z. Liu, S. P. Lau and F. Yan, *Chemical Society Reviews*, 2015, **44**, 5638-5679.

165. D. Jariwala, V. K. Sangwan, L. J. Lauhon, T. J. Marks and M. C. Hersam, *Chemical Society Reviews*, 2013, **42**, 2824-2860.

166. C. Hu, Y. Wang, S. Chen, H. Cheng, M. Lin, Y. Zhang, D. He, X. Liu and J. Liu, *RSC Advances*, 2016, **6**, 78053-78058.

167. J. Zhang, X. Liu, G. Neri and N. Pinna, *Advanced Materials*, 2016, **28**, 795-831.
168. D. R. Kauffman and A. Star, *Angewandte Chemie International Edition*, 2008, **47**, 6550-6570.
169. X. Chen, B. Guo, P. Hu and Y. Wang, *Electroanalysis*, 2014, **26**, 1513-1521.
170. K. Balasubramanian and K. Kern, *Advanced Materials*, 2014, **26**, 1154-1175.
171. C. Zhou, J. Zhao, J. Ye, M. Tange, X. Zhang, W. Xu, K. Zhang, T. Okazaki and Z. Cui, *Carbon*, 2016, **108**, 372-380.
172. L. Dang, G. Zhang, K. Kan, Y. Lin, F. Bai, L. jing, P. Shen, L. Li and K. Shi, *Journal of Materials Chemistry A*, 2014, **2**, 4558-4565.
173. D. Wan, S. Yuan, G. L. Li, K. G. Neoh and E. T. Kang, *ACS Applied Materials & Interfaces*, 2010, **2**, 3083-3091.
174. M. Khan and S.-Y. Park, *Analytical Chemistry*, 2014, **86**, 1493-1501.
175. M. Seol, D. H. Youn, J. Y. Kim, J.-W. Jang, M. Choi, J. S. Lee and K. Yong, *Advanced Energy Materials*, 2014, **4**, n/a-n/a.
176. F. Yao, D. T. Pham and Y. H. Lee, *ChemSusChem*, 2015, **8**, 2284-2311.
177. Q. Zhang, J.-Q. Huang, W.-Z. Qian, Y.-Y. Zhang and F. Wei, *Small*, 2013, **9**, 1237-1265.
178. D. Li, Y. Gong and C. Pan, *Scientific Reports*, 2016, **6**, 29788.
179. Y. Wang, B. Fugetsu, Z. Wang, W. Gong, I. Sakata, S. Morimoto, Y. Hashimoto, M. Endo, M. Dresselhaus and M. Terrones, *Scientific Reports*, 2017, **7**, 40259.
180. L. Liu, Z. Niu and J. Chen, *Chemical Society Reviews*, 2016, **45**, 4340-4363.
181. P. Wu, S. Cheng, L. Yang, Z. Lin, X. Gui, X. Ou, J. Zhou, M. Yao, M. Wang, Y. Zhu and M. Liu, *ACS Applied Materials & Interfaces*, 2016, **8**, 23721-23728.
182. Y. Zhang, B. Lin, J. Wang, J. Tian, Y. Sun, X. Zhang and H. Yang, *Journal of Materials Chemistry A*, 2016, **4**, 10282-10293.
183. X. Zhou, A. Wang, Y. Pan, C. Yu, Y. Zou, Y. Zhou, Q. Chen and S. Wu, *Journal of Materials Chemistry A*, 2015, **3**, 13011-13015.
184. T. Peng, H. Yi, P. Sun, Y. Jing, R. Wang, H. Wang and X. Wang, *Journal of Materials Chemistry A*, 2016, **4**, 8888-8897.
185. J. Liu, C. Wang, X. Wang, X. Wang, L. Cheng, Y. Li and Z. Liu, *Advanced Functional Materials*, 2015, **25**, 384-392.

186. I. Marangon, C. Ménard-Moyon, J. Kolosnjaj-Tabi, M. L. Béoutis, L. Lartigue, D. Alloyeau, E. Pach, B. Ballesteros, G. Autret, T. Ninjbadgar, D. F. Brougham, A. Bianco and F. Gazeau, *Advanced Functional Materials*, 2014, **24**, 7173-7186.

187. L. Cabana, M. Bourgognon, J. T. W. Wang, A. Protti, R. Klippstein, R. T. M. de Rosales, A. M. Shah, J. Fontcuberta, E. Tobías-Rossell, J. K. Sosabowski, K. T. Al-Jamal and G. Tobias, *Small*, 2016, **12**, 2893-2905.

188. J. T.-W. Wang, L. Cabana, M. Bourgognon, H. Kafa, A. Protti, K. Venner, A. M. Shah, J. K. Sosabowski, S. J. Mather, A. Roig, X. Ke, G. Van Tendeloo, R. T. M. de Rosales, G. Tobias and K. T. Al-Jamal, *Advanced Functional Materials*, 2014, **24**, 1880-1894.

189. S. Y. Hong, G. Tobias, K. T. Al-Jamal, B. Ballesteros, H. Ali-Boucetta, S. Lozano-Perez, P. D. Nellist, R. B. Sim, C. Finucane, S. J. Mather, M. L. H. Green, K. Kostarelos and B. G. Davis, *Nat Mater*, 2010, **9**, 485-490.

190. C. Spinato, A. Perez Ruiz de Garibay, M. Kierkowicz, E. Pach, M. Martincic, R. Klippstein, M. Bourgognon, J. T.-W. Wang, C. Menard-Moyon, K. T. Al-Jamal, B. Ballesteros, G. Tobias and A. Bianco, *Nanoscale*, 2016, **8**, 12626-12638.

191. X. Liu, I. Marangon, G. Melinte, C. Wilhelm, C. Ménard-Moyon, B. P. Pichon, O. Ersen, K. Aubertin, W. Baaziz, C. Pham-Huu, S. Bégin-Colin, A. Bianco, F. Gazeau and D. Bégin, *ACS Nano*, 2014, **8**, 11290-11304.

# Chapter 2 Characterization Techniques

The main objective of the present work is the synthesis and characterization of magnetic nanomaterials with different nanostructures, for applications in a variety of chemical and biochemical areas. For their appropriate use in these different applications, different kinds of characterization techniques are used in the present thesis. In this chapter, brief introductions about characterization techniques is presented.

## 2.1 Thermogravimetric Analysis (TGA)

To quantify the organic compound in the synthesized nanocomposites, thermogravimetric analysis technique was used in this work. Thermogravimetric Analysis (TGA) is a technique where the mass of sample is monitored as a function of temperature or time when the sample specimen is subjected to an environment with controlled temperature and atmosphere. TGA consists of a sample pan which resides in a furnace and is heated or cooled during the experiment and the mass of the sample can be monitored by a precision balance during the experiment. The temperature and weight change of decomposition reactions, which allows quantitative composition analysis, can be determined via TGA techniques.[1]

The TGA can also be combined with the differential scanning calorimetry (DSC) technique. The DSC analyzer measures the energy changes that occur as a sample is heated, cooled or held

isothermally, together with the temperature at which these changes occur. The energy changes enable characterize the transitions that happen in the sample quantitatively, such as melting processes, glass transitions and crystallization.[2]

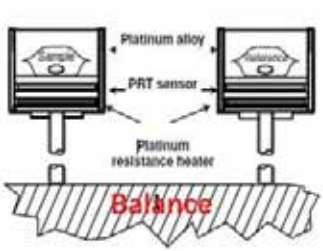


**Figure 2.1 Scheme of TGA-DSC instrument set up[2]**

The TGA tests in present thesis were carried on a NETZSCH-STA 449 F1 Jupiter thermal analysis system from room temperature to 800ºC under a $O_2$ flow.

# 2.2 X-Ray Diffraction (XRD)

The crystal structure and phase information are very important features of nanomaterials, which relate to their physical properties such as magnetic, electronic and optical properties. Due to its advantages in the crystal analysis, X-ray Diffraction is perhaps the most widely used technique for characterizing materials. When x-ray photons interact with a solid material, some photons did not lose any energy, the process is called elastic scattering (Thompson Scattering). These diffracted waves from different atoms can interfere with each other which will strongly modulate the

resultant intensity distribution. If the atoms are arranged in a periodic fashion in the solid materials, for instance in crystals, the diffracted waves will consist of sharp peaks with the special symmetry determined by the distribution of atoms. So, the distribution of atoms in solid material can be deduced by measuring the diffraction patterns.[3-5]

The relationship describing the angle of X-rays and the wavelength diffracts from a crystalline surface was discovered by Sir William H. Bragg and Sir W. Lawrence Bragg and is known as Bragg's Law[6]

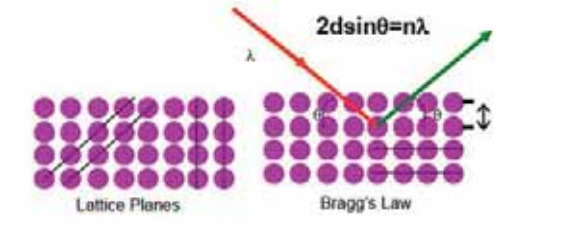


**Figure 2.2 Scheme of Bragg's Law**

**2dsinθ=nλ** (λ=wavelength of the x-ray, θ=scattering angle, n=integer representing the order of the diffraction peak., d=inter-plane distance of (i.e atoms, ions, molecules)

In this thesis, X-ray powder diffraction studies (XRD) were performed on D5000 Siemens X-Ray powder diffractometer in a reflection mode by using Cu Kα λ=1.5406 Å radiation in a range of $10° \leq 2\theta \leq 80°$.

# 2.3 Infrared spectroscopy (IR)

Nanomaterials prepared for different applications need surface modification to make them suitable for their use in different environments, this surface consists, usually, for ligand stabilized nanoparticles in organic molecules. For this reason, a well understanding about the surface functional group on the nanocomposite is essential for obtaining desired nanomaterials. So, infrared spectroscopy (IR) technique is used for the surface characterization.

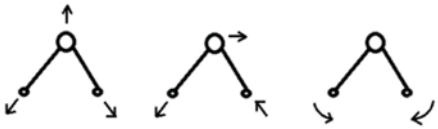

**Figure 2.3 Different vibration models of molecules.**

Infrared spectroscopy is a technique to analyze the structure of organic molecules by using a beam of infrared light. Molecules in solids are always in vibration at their equilibrium status and those vibrations can be classified into the form of stretching and bending (Figure 2.6). When a molecule is irradiated by infrared light, a specific frequency may match the vibrational frequency of the molecule ($\nu_{vib}$), consequently, the molecular vibration will be excited by waves with the frequency $\nu_{ph}=\nu_{vib}$ and the light will be strongly absorbed. In this way, the frequency of the absorption peak is determined by the vibrational energy gap, the number of absorption peaks is related to the number of vibrational freedom of the molecule and the intensity of absorption peaks is related to the change of dipole moment and the possibility of the transition of energy levels. Therefore, the

abundant fingerprint information about the chemical composition of the molecules can be obtained by analyzing the infrared absorption spectrum.[7-9]

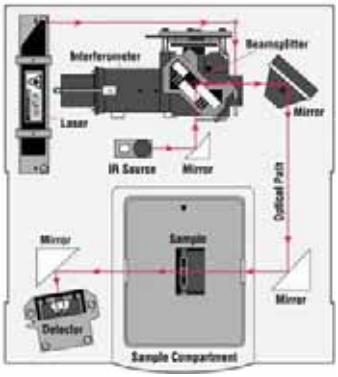


**Figure 2.4 Scheme of a IR instrument set up**

In this thesis, Fourier transform infrared spectroscopy (ATR-FT-IR) was performed on a Bruker Tensor 27 Fourier transform infrared spectrometer (Golden gate) in a range of 600-4000$cm^{-1}$. All samples were measured in solid form at room temperature.

# 2.4 Ultraviolet-Visible Spectroscopy（UV-Vis）

Ultraviolet-visible spectroscopy has been used by chemists for a long time and was really one of the first spectroscopic techniques developed in the world. As it is known to all, light is a form of energy, the absorption of light by sample causes the energy content of the molecules (or atoms) to increase. In some molecules and atoms, photons of UV or visible light have enough energy to

cause an electron from a lower energy level to a higher energy level. (excitation of electrons). The absorbance of light will be proportional to the number of absorbing molecules (or atoms). By comparing the intensity of light transmitted through the sample and reference control (Figure 2.8), the absorbance of light can be determined, which is very useful for chemistry and materials science analysis for example concentration determination, rates of reaction calculation and the study of reaction mechanism.[10-13] For the reasons above, UV-vis test was used in our study for analyzing catalytic reactions. In the particular case of nanoparticles it is possible to establish, in some cases a relationship between their size and aspect and the UV measurements (Plasmon effect).[14]

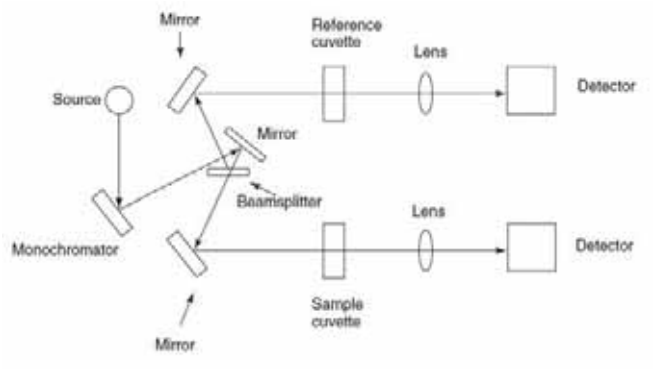


**Figure 2.5 Scheme of a UV-Vis spectrometer set up**

In the present study, a Varian Cary 5000 UV-Vis-NIR spectrophotometer was operated at 1nm resolution using freshly made solution in quartz cuvettes with 10mm path length.

# 2.5 Transmission electron microscopy (TEM)

The particle size, morphology and crystal structure are very important parameters of nanomaterials. The use of electron microscopes would be necessary for materials science, especially in the research about nanomaterials. To obtain detail information, TEM techniques would be an ideal candidate to obtain that information. Today TEM is the most efficient and versatile tool for the characterization of materials over spatial ranges from the atomic scale, through the ultra-small nanometer level (from < 1nm to 100 nm) up to the micrometer level and beyond. It is a microscopy technique where a beam of electrons is transmitted through an ultra-thin specimen, interacting with the atoms of the sample as it passes through it.[15] As it shown in Figure 2.1, the interactions between the electrons and the atoms of samples can be divided into different kind of signals which can be used to analysis features of samples such as the crystal structure, morphologies and element composition.[16]

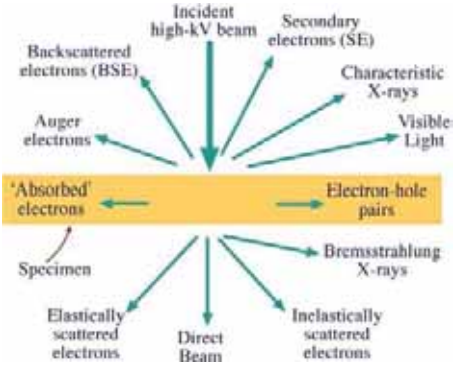


**Figure 2.6 Signals generated when a high-energy beam of electrons interacts with a thin specimen**

According to the way to apply the electrons beam to samples, TEM can be classified to conventional TEM (CTEM) and scanning TEM (STEM).[17] In CTEM, a relative wide electron beam which is close to parallel is applied to the whole area of sample and the image signals were also collected in parallel and simultaneously (Figure 2.2). Whereas, in STEM equipment, a very fine and focused electron beam was used as the probe to scan across the whole or selected area of sample pixel by pixel and the signals were also obtained by specific detectors point by point (Figure 2.2). The image resolution of CTEM instrument is primarily determined by the aberrations in the objective lens, whilst the image resolution of STEM instrument is determined mainly by the beam diameter generated by the probe-forming lens which is also limited by aberrations. [18]

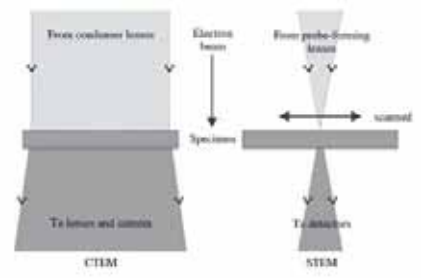


**Figure 2.7 The electron beam in CTEM and STEM instruments**

The sample suitable for study by TEM should obviously be thin enough for electron transmission, and representative of the materials. The ideal samples must fit the following requirements:[18]

• electron beam spreading within the specimen is negligible;

• if the sample is nanoparticle, it should be able to be supported on a thin substrate with the total

thickness still small enough to satisfy the constraint above;

• it is self-supporting over a region large enough to find the features of interest

• surface contamination does not dominate the signal

• there is sufficient signal from scattering events to give statistically significant (i.e. low noise or high enough signal to noise ratio) images or spectra.

The TEM test in the present studies, JEOL 1210 TEM microscopy at 130kv, JEM-2011 HR-TEM microscopy at 200kv and FEI Tecnai G2 F20 S-TWIN HR(S) TEM at 200kv were used.

# 2.6 Electron energy-loss spectrometry (EELS) and energy dispersive X-ray analysis (EDX)

For elemental and chemical analysis, inelastic processes such as: Phonon scattering, Plasmon scattering, Single electron excitation and Direct Radiation Losses are concerned. In this thesis, electron energy-loss spectrometry (EELS) and energy dispersive X-ray analysis (EDX) analysis were carried out in a FEI Tecnai F20 S/TEM system.

When a high-energy electron beam traverses a sample, the electrons can either emerge unscathed or lose energy through a variety of processes. Electron energy loss spectrometry (EELS) is an absorption spectroscopy in which the energy losses of the incident electrons following transmission through the sample were measured.[19] In a EELS instrument (Figure 2.3), a typical

sector magnet consists of a homogeneous magnetic field normal to the electron beam was added to the end of TEM column. This magnetic field causes electrons with different energy (and therefore energy loss) bent to specific angles respectively result to a spatially dispersed phenomenon. By measuring those electrons, the information about the element composition of the sample can be collected. [19-21]

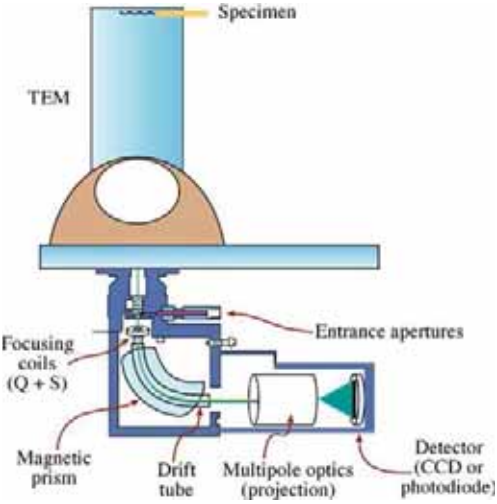


**Figure 2.8 Scheme of a EELS instruments is combined with a TEM column**

Apart from the EELS, X-rays can be generated because of the interaction between incident electrons and sample atoms. The difference of the emitted X-rays photons energy can be attributed to the different excited states which are the characteristics of the sample atoms. By analyzing the energy difference of X-rays and calculate the intensity of the emitted X-rays, elemental identification and quantification can be achieved. [21]In a EDX detector, when X-rays deposit energy

in the Si semiconductor layer of the detector, electrons are transferred from valence band to conduct band results in the formation of electron-hole pairs. As it is known before, the energy for accomplish this electron transfer process in Si is 3.8eV under liquid N2 temperature. The number of the electron-hole pairs can be measured which is directly proportional to the energy of the X-rays photons. In this way, the information of the composition can be obtained. [3] The components and location of an EDX detector are shown in Figure 2.4.

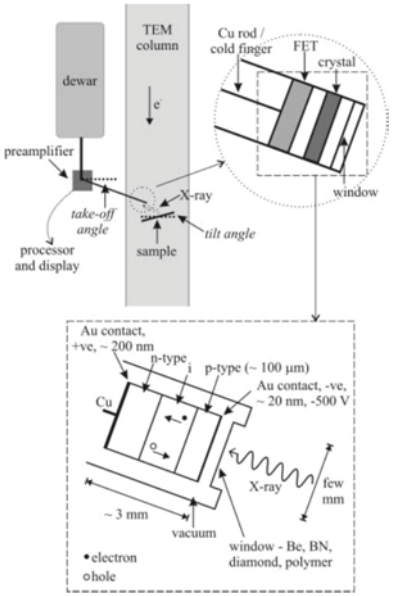


**Figure 2.9 Scheme of the components and location of an EDX detector in a TEM**

# 2.7 Superconducting quantum interference devices (SQUIDs)

The magnetic behaviors of the synthesized nanomaterials are essential properties for their application in many different areas. The Superconducting Quantum Interference Device (SQUID) utilizes the physical phenomena of flux quantization and D.C Josephson effect to characterize the magnetic properties of sample.

When a superconducting ring remains in the superconducting state, the magnetic flux within it remains trapped. This trapped flux cannot be changed the level of magnetic flux in a continuous manner and can only be trapped in the discrete levels which mean that the magnetic flux is quantized and exists only in multiples of the flux quantum. According to the previous study, the field inside the superconducting ring with an area of $1cm^2$ can only exist in discrete steps of $2.068*10^{-11}T$.[22] This phenomena can be called flux quantization .

When two superconducting rings are coupled weakly. A Josephson junction (JJ) will be formed via placing an insulating gap between the two superconductors. If the gap is thin enough, electron pairs can tunnel from one superconductor through the gap to the other superconductor. By quantum tunneling, a no-resistance current can flow across the insulator. This is effect called the D.C Josephson effect, which is a demonstration of long-range quantum coherence of superconductors.[23]

A typical SQUID instrument has a ring of superconductor interrupted by one or more Josephson

junctions. When an external magnetic flux is coupled into the SQUID loop, the voltage across the Josephson junction will change. By monitoring the changing of the voltage allows determination of the external magnetic flux can be determined to reveal the magnetic properties of the sample. [24] It is worth to mention that the magnetic saturation value is only related to the magnetic composites in the bulk materials. This property can be applied to determine the percentage of the magnetic materials in whole bulk materilas.

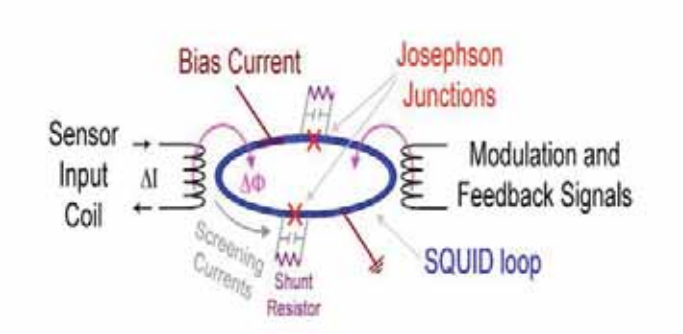


**Figure 2.10 Scheme of SQUID instrument**

In this thesis, the field-dependent magnetization curves were characterized by SQUID (Quantum design MPMS XL-7T) under a magnetic field from 0 to ±70000Oe at 5K.

# References


1. Bottom, R., Thermogravimetric Analysis. In *Principles and Applications of Thermal Analysis*, Blackwell Publishing Ltd: 2008; pp 87-118.
2. Gabbott, P., A Practical Introduction to Differential Scanning Calorimetry. In *Principles and*

*Applications of Thermal Analysis*, Blackwell Publishing Ltd: 2008; pp 1-50.

3. Williams, D. B.; Carter, C. B., X-ray Spectrometry. In *Transmission Electron Microscopy: A Textbook for Materials Science*, Springer US: Boston, MA, 2009; pp 581-603.
4. Jenkins, R.; Snyder, R. L., Diffraction Theory. In *Introduction to X-ray Powder Diffractometry*, John Wiley & Sons, Inc.: 1996; pp 47-95.
5. Leng, Y., X-Ray Diffraction Methods. In *Materials Characterization*, Wiley-VCH Verlag GmbH & Co. KGaA: 2013; pp 47-82.
6. Welzel, U.; Mittemeijer, E. J., Laboratory Instrumentation for X-Ray Powder Diffraction: Developments and Examples. In *Modern Diffraction Methods*, Wiley-VCH Verlag GmbH & Co. KGaA: 2012; pp 359-398.
7. Leng, Y., Vibrational Spectroscopy for Molecular Analysis. In *Materials Characterization*, Wiley-VCH Verlag GmbH & Co. KGaA: 2013; pp 283-332.
8. Williamson, K. L.; Masters, K. M., *Macroscale and microscale organic experiments*. Cengage Learning: 2010.
9. How an FTIR Works. In *Fundamentals of Fourier Transform Infrared Spectroscopy, Second Edition*, CRC Press: 2011; pp 19-53.
10. Stuart, B. H., Molecular Spectroscopy. In *Analytical Techniques in Materials Conservation*, John Wiley & Sons, Ltd: 2007; pp 109-208.
11. Patonay, G.; Beckford, G.; Hänninen, P., UV–Vis and NIR Fluorescence Spectroscopy. In *Handbook of Spectroscopy*, Wiley-VCH Verlag GmbH & Co. KGaA: 2014; pp 999-1036.
12. Tissue, B. M., Ultraviolet and Visible Absorption Spectroscopy. In *Characterization of Materials*, John Wiley & Sons, Inc.: 2002.
13. Primer, A., Fundamentals of UV-visible spectroscopy. *Copyright Hewlett-Packard Company, Hewlett-Packard publication* 1996.
14. Eustis, S.; El-Sayed, M. A., Why gold nanoparticles are more precious than pretty gold: Noble metal surface plasmon resonance and its enhancement of the radiative and nonradiative properties of nanocrystals of different shapes. *Chemical Society Reviews* 2006, 35, 209-217.
15. Fultz, B.; Howe, J., The TEM and Its Optics. In *Transmission Electron Microscopy and Diffractometry of Materials*, Springer Berlin Heidelberg: Berlin, Heidelberg, 2013; pp 59-

115.

16. Williams, D. B.; Carter, C. B., The Transmission Electron Microscope. In *Transmission Electron Microscopy: A Textbook for Materials Science*, Springer US: Boston, MA, 2009; pp 3-22.
17. Introduction. In *Transmission Electron Microscopy: Physics of Image Formation*, Springer New York: New York, NY, 2008; pp 1-15.
18. Goodhew, P., General Introduction to Transmission Electron Microscopy (TEM). In *Aberration-Corrected Analytical Transmission Electron Microscopy*, John Wiley & Sons, Ltd: 2011; pp 1-19.
19. Egerton, R. F., An Introduction to EELS. In *Electron Energy-Loss Spectroscopy in the Electron Microscope*, Springer US: Boston, MA, 2011; pp 1-28.
20. Williams, D. B.; Carter, C. B., Electron Energy-Loss Spectrometers and Filters. In *Transmission Electron Microscopy: A Textbook for Materials Science*, Springer US: Boston, MA, 2009; pp 679-698.
21. Brydson, R.; Hondow, N., Electron Energy Loss Spectrometry and Energy Dispersive X-ray Analysis. In *Aberration-Corrected Analytical Transmission Electron Microscopy*, John Wiley & Sons, Ltd: 2011; pp 163-210.
22. Fagaly, R. L., Superconducting quantum interference device instruments and applications. *Review of Scientific Instruments* 2006, 77, 101101.
23. Chesca, B.; Kleiner, R.; Koelle, D., SQUID Theory. In *The SQUID Handbook*, Wiley-VCH Verlag GmbH & Co. KGaA: 2005; pp 29-92.
24. Cantor, R.; Ludwig, F., SQUID Fabrication Technology. In *The SQUID Handbook*, Wiley-VCH Verlag GmbH & Co. KGaA: 2005; pp 93-125.

# Chapter 3 Results Compilation of Articles

In this chapter, the results derived from the thesis work are presented as a compilation of articles. An extended abstract is prepared for each article. The general discussion of the results can be found in the articles themselves.

# 3.1 Ultra-fast microwave assistance reverse microemulsion synthesis of $Fe_3O_4$@$SiO_2$ core-shell nanoparticles as a highly recyclable silver nanoparticles catalytic platform in the reduction of 4-nitroaniline

## 3.1.1 Introduction

There's Plenty More Room at the Bottom——Richard Phillips Feynman

Nowadays, the uniform nanoparticles with controlled shape and size distribution play a fundamental role in many areas of science and technology. The use of nanoparticles as building blocks to form 1-,2-, and 3-diemsional arrays with complex structure provide us an extending view to novel functional materials research and development.[1] Among thousands of kinds of nanoparticles, the core-shell structure nanoparticles attract many attention and intensively studied for their promising property which is the ability to achieve different functional application in one single particles. Not only limited to their applications in variety areas, the core-shell nanoparticles can also represent a major inspiration to us for designing and preparation of new kind of nanomaterials for human goods. As a key part of nanoscience, core-shell nanoparticles will still need investigation to get further well understanding about these nanomaterials and find out

efficient strategies when facing many social problems such as novel light source, new catalysts for chemical reactions, highly efficient medical products for different disease and alternative energy issues.

# 3.1.1.1Core-shell nanoparticles

A general classification can be done for nanoparticles according to their geometrical morphology which are solid nanoparticles, hollow nanoparticles and core-shell nanoparticles. Normally, core-shell nanoparticles often refer to a solid or hollow nanoparticle coated with a thin shell.

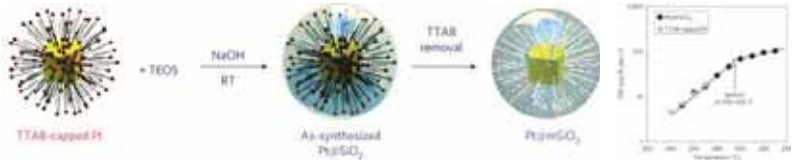


**Figure 3.1 Example of the application of the Pt@$SiO_2$ core-shell nanoparticles for CO oxidation reaction[2]**

Compare to the solid and hollow nanoparticles, core-shell nanoparticles are gradually attracting more and more attention because of the combination of specific properties of core and shell materials. Because of the shell coating, the properties of core materials could be modified such as thermal stability and dispersibility, in the meanwhile the coating of different materials would make the products more easily to be functionalized with other molecules and nanoparticles. With this special advantages, core shell nanoparticles are widely used in biomedical research[3], catalysis[4],

electronic device[5], photoluminescence research[6, 7].

## 3.1.1.2 Classification of core-shell nanoparticles

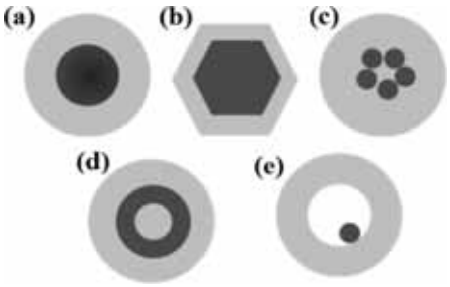


**Figure 3.2 Different types of core/shell nanoparticles: (a) spherical core/shell nanoparticles; (b) hexagonal core/shell nanoparticles; (c) multiple small core materials coated by single shell material; (d) nanomatrioshka material; (e) movable core within hollow shell material[8]**

A classification of core/shell nanoparticles is shown schematically in Figure 4.2. The spherical core/shell nanoparticles are the most common (Figure 4.2a) where a spherical core nanoparticle is completely coated by a shell of different materials. Different shaped core/shell nanoparticles are generally formed when a core is nonspherical as shown in Figure 4.2b which also given rise to immense research interest because of their novel properties. Multiple core core/shell nanoparticles are formed when a single shell material is coated onto many small core concennanoparticles together as shown in Figure 4.2c. Multi-shell core-shell nanoparticles are synthesized via alternative coating of dielectric core and metal shell material onto each other (A/B/A type) (Figure 4.2). Here nanoscale dielectric spacer layers separate the concentric metallic layers These types of

core-shell nanoparticles are very important for their plasmonic properties[9]. It is also possible to synthesize a smaller core particle with a uniformed hollow shell outside the particle (Figure 4.2e) after a bilayer coating of the core material and just removing the first layer by using a suitable process. [8]

## 3.1.1.3 Synthesis of core-shell nanoparticles

Like the synthesis of normal nanoparticles, methodology for core-shell nanomaterials synthesis can be generally divided into two categories: “top-down” and “bottom-up”. The “top-down” approach often uses traditional microfabrication methods where externally controlled tools are used to cut, mill or shape the materials into the desired shape, order and structure. For example, the most widely used techniques are lithographic techniques (e.g., UV, electron or ion beam, scanning probe, optical near field)[10, 11], laser-beam processing[12-14] and mechanical techniques (e.g., machining, grinding, and polishing)[15-17]. On the other hand, the “Bottom-up” methods exploit the chemical properties of the molecules to make them to self-assemble into the desired nanostructures. The most common bottom-up approaches are chemical synthesis, chemical vapor deposition, laser-induced assembly, self-assembly and colloidal aggregation etc[18-22]. Nowadays, when compared with the top-down approach the bottom-up approach can produce much smaller sized nanoparticles in a more cost-effective way with the advantages of absolute precision, complete control over the process, and minimum energy loss. Since ultimate control is required for achieving highly stable core nanoparticles and a uniform coating of the shell materials during the formation of cores-shell nanoparticles, the bottom-up approach has proven more suitable. A combination of these two approaches can also be utilized, for example when the core particles were synthesized

by the top-down approach while then coated by a bottom-up approach in order to get the shell with a uniform and precisely controlled thickness. It is worth to mention that in order to control the overall size and shell thickness more precisely, instead of employing a bulk medium, using microemulsion or reverse microemulsion method is preferable because the oil or water droplets will act as a template and the nanoreactor during the preparation of core-shell nanostructures[23-25].

# 3.1.1.4 Introduction of the article

$Fe_3O_4$@$SiO_2$ core/shell nanoparticles are one of most promising candidates for biomedicine applications, catalysis and electronic device because of their magnetic properties and easy functionalized silica surface. For the preparation of $Fe_3O_4$@$SiO_2$ core-shell nanoparticles the normal Stober method and reverse emulsion process both need a long time to form $SiO_2$ layer which is a great disadvantage that hinders the fast and massive production of $Fe_3O_4$@$SiO_2$ core/shell nanoparticles and their wide application. With the combination of microwave irradiation, the core-shell nanoparticles could be obtained in only a few minutes. Although there are some papers using microwave assistance Stober Method to fabricate core-shell nanoparticles, they always obtain big size nanoparticles with very thick silica shell.

A promising strategy is combining the fast microwave process with a controllable reverse microemulsion method. The products we got can be controlled to monodisperse single-core core-shell nanoparticles with very thin $SiO_2$ layer. Although the microwave and reverse microemulsion were widely used in the preparation of nanomaterials, the combination of both methods was rarely reported, up to now only few papers using microwave assistance reverse microemulsion method

to synthesize Au NPs, microporous zinc phosphates, zeolite nanocrystals and metal organic framework. Using this strategy to fabricate core-shell nanoparticles hasn't been reported yet. It is reasonable to believe that this method is promising for massive production of $Fe_3O_4$@$SiO_2$ core/shell nanoparticles and other kinds of nanocomposites with complex structure.

In this paper, $Fe_3O_4$@$SiO_2$ core-shell nanoparticles were synthesized through the combination of microwave irradiation and reverse microemulsion method for the first time. The obtained nanoparticles were used as solid supports for Ag nanoparticles catalysts shown great catalytic and recycling properties. The results of the fully characterization of synthesized core-shell nanoparticles revealed that the morphology of core-shell nanoparticles can be well manipulated via changing the reaction parameters. The results of TEM test of $Fe_3O_4$@$SiO_2$/Ag nanocomposites indicated that the core-shell nanoparticles were well decorated with Ag nanocrystals which has a narrow size distribution. These synthesized $Fe_3O_4$@$SiO_2$/Ag nanocomposites shown great catalytic property because of the high surface activity of Ag nanoparticles and the large surface area supplied by core-shell nanoparticles. The recycling test also indicated that these materials have good reutilization property. We believe this new method and materials promising for core-shell nanoparticles preparation and application in catalysis, biomedicine and energy science research.

RSC Advances

PAPER

View Article Online
View Journal | View Issue



Cite this: *RSC Adv.*, 2016, **6**, 88762

# Ultra-fast microwave-assisted reverse microemulsion synthesis of $Fe_3O_4$@$SiO_2$ core–shell nanoparticles as a highly recyclable silver nanoparticle catalytic platform in the reduction of 4-nitroaniline†

C. Y. Lu,*[ab] T. Puig,[b] X. Obradors,[b] S. Ricart[b] and J. Ros[a]

Received 1st August 2016
Accepted 12th September 2016

DOI: 10.1039/c6ra19435d

www.rsc.org/advances

A novel microwave-assissted reverse microemulsion method was applied to prepare $Fe_3O_4$@$SiO_2$ core–shell nanoparticles rapidly for the first time. The morphology of the core–shell structure is controlled by tunning the reaction parameters. Nanoparticles with a very thin $SiO_2$ coating layer (2.5 nm) containing a single $Fe_3O_4$ nanoparticle (8–9 nm) are produced. These core–shell nanoparticles can be used as solid catalytic supports for Ag nanoparticles and applied in 4-nitroaniline reduction. Transmission electron microscopy showed that the core–shell nanoparticles were decoracted with Ag nanoparticles of 7 nm in diameter. The crystal structures of the $Fe_3O_4$ and Ag nanoparticles were confirmed by X-ray diffraction. These Ag/$Fe_3O_4$@$SiO_2$ nanocomposites showed high catalytic efficiency and recycling properties even after 20 times of repetation.

## Introduction

Due to their unique magnetic properties and biocompatibility, iron oxide nanoparticles have been intensively studied for the past few decades for wide applications in biotechnology, data storage, magnetic fluids and catalysis.[1,2] Nobel metal nanomaterials, like Au, Pt and Ag, are promising catalysts for many reactions, for example Au nanoclusters can be used in the selective oxidation of styrene[3] and Pt-based heterogeneous nanomaterials are promising catalysts in direct methanol fuel cells.[4] Ag nanoparticles have also been comprehensively studied for their promising application in biotechnology and catalysis. Compared with other noble metal nanoparticles, such as Au, Pt and Pd, Ag nanoparticles are cheaper and have some special properties like antibacterial activity, plasmon resonant optical properties and an enhancing the effect of radiation treatment, which make them ideal candidates for biomarkers, optical sensors and antimicrobial drugs.[5,6] It is also worth noting that using Ag NPs as the catalyst to reduce nitroaniline would be an effective and environmentally friendly procedure to synthesize amino compounds.[7]

Because of the multifunctional requirement, $Fe_3O_4$/Ag composite materials with the combination of excellent magnetic properties, biocompatibilities and plasmonic properties would be a promising composite for multiple applications. However the uncovered $Fe_3O_4$ NPs were easy to oxidized and aggregated during the preparation and application process. The chemical and thermal stable silica layers could be a nice candidate for decorating and protect the iron oxide nanoparticles' surface. And the nontoxic silica provides $Fe_3O_4$ nanoparticles with water solubility as well as good biocompatibility, which has potential applications in bio-imaging and drug delivery.[8] For the research in functional materials, $Fe_3O_4$@$SiO_2$@$Y_2O_3$:$Eu_3^+$ core–shell structures have magnetic response performance and luminescent properties[9] and the $Fe_3O_4$@$SiO_2$@Au core–shell microspheres exhibit an enhancement ability of surface-enhanced Raman scattering for rhodamine-b detection.[10]

Nowadays, Stöber method[11–16] and reverse microemulsion system[17–24] were both widely used to prepare $Fe_3O_4$@$SiO_2$ core–shell structures. $Fe_3O_4$@$SiO_2$ core–shell nanoparticles with ultra-thin silica shell (~2 nm) and a high saturated magnetization (15 emu $g^{-1}$)[25] can be synthesized through reverse microemulsion method.[26–28] However, both methods requires long time for $SiO_2$ condensing, taking around 24 h for one reaction.[29] This is a great disadvantage that hinders the fast and massive production of $Fe_3O_4$@$SiO_2$ core/shell nanoparticles and their wide application.

[a]*Departament de Química, Edifici C Facultat de Ciències, Universitat Autònoma de Barcelona (UAB), Cerdanyola del Vallès, Barcelona 08193, Spain. E-mail: lu.changyong@e-campus.uab.cat*

[b]*Institute of Materials Science of Barcelona (ICMAB-CSIC), Campus de la UAB, Cerdanyola del Vallès, Barcelona 08193, Spain*

† Electronic supplementary information (ESI) available: Electron diffraction pattern, thermal gravity cure, weight percentage calculation and elements mapping test. See DOI: 10.1039/c6ra19435d

Microwave irradiation significantly accelerates the reaction rate, increases yields and reduces side reactions in the preparation of different kinds of nanoparticles, from metals to oxides and semiconductors.[30–32] The synthesis of NPs@$SiO_2$ core–shell structure were only reported by using microwave assistance Stöber method,[33,34] and the fast preparation of core–shell nanoparticles with controllable small size and very thin $SiO_2$ layer remain challenging. The combination of microwave irradiation and reverse microemulsion method has the possibility to overcome this problem, to our knowledge, this method was used until now to prepare Au NPs, zincophosphates,[35] MOF[36] and zeolite nanocrystals[37] and the results indicate that this method has great improvement on yield, size distribution and reducing the reaction than the normal reverse microemulsion method.

In this work, we report a novel rapid approach based on microwave assisted reverse microemulsion process to synthesize $Fe_3O_4$@$SiO_2$ core–shell nanoparticles with a very thin $SiO_2$ layer (2.5 nm in average) within only 5 min (Fig. 1). The synthesized core–shell structures were stable in ethanol and well-formed. Moreover these $Fe_3O_4$@$SiO_2$ core–shell nanoparticles were further functionalized with (3-aminopropyl)triethoxysilane (APTES) and decorated with Ag nanoparticles. The morphology and crystal structure of $Fe_3O_4$@$SiO_2$ and $Fe_3O_4$@$SiO_2$/Ag nanoparticles were analysed through different techniques for example transmission electron microscopy (TEM), high resolution transmission electron microscopy (HR-TEM) and X-ray diffraction (XRD) and the magnetic properties were measured by superconducting quantum interference device (SQUID). The catalytic efficiency and recycling test were done *via* monitoring the 4-nitroaniline reduction reaction. The morphology of nanoparticles, such as the aggregation and the number of core particles, can be well manipulated through changing the amount of reactants. This kind of core–shell nanoparticle is superparamagnetic with a relatively high saturation magnetization value 32.7 emu $g^{-1}$.[27] This kind of core–shell nanoparticle could be used as the support for Ag nanoparticles and the synthesized $Fe_3O_4$@$SiO_2$/Ag nanocomposites show great catalytic and recycling properties.

## Experimental details

### Materials

Iron(III) acetylacetonate (99.9%), benzyl ether (98%), oleic acid (90%), oleylamine (70%), triethylene glycol (99%), cyclohexane (99%), Igepal CO-520 (average $M_n$ 441), ammonium hydroxide solution (30–33% $NH_3$ in $H_2O$), tetraethyl orthosilicate (98%), (3-aminopropyl)triethoxysilane (APTES, 99%), sodium borohydride (98%), silver nitrate (99%) and 4-nitroaniline (99%) were used as received from Sigma-Aldrich (Madrid Spain). *n*-Hexane (96%) was used as received from Scharlab (Barcelona Spain). Ethanol (absolute PA 99.5%) was used as received from PanReac AppliChem (Barcelona Spain).

### Synthesis of $Fe_3O_4$ nanoparticles

The oleic acid and oleylamine capped $Fe_3O_4$ nanoparticles were prepared through a modified way of the decomposition of iron oleate complex described somewhere else.[1] In a typical synthesis, 1 mmol iron(III) acetylacetonate was dissolved in 20 ml benzyl ether then 3 mmol oleic acid, 3 mmol oleylamine and 5 mmol triethylene glycol were subsequently added into the solution, followed by transfer the mixture to a two neck round bottom flask with magnetically stirred under $N_2$ flow for at least 30 min to eliminate the oxygen inside the vial. The mixture was heated to 200 °C at heating rate 1 °C $min^{-1}$ and kept for 30 min. Then the mixture was heated to 265 °C under the same heating rate and hold for another 30 min. The black solution was cooled to room temperature naturally. All the experiments were under refluxing process and $N_2$ flow. The $Fe_3O_4$ nanoparticles were precipitated by adding ethanol, collected by centrifugation (10 000 rpm, 10 min) and dispersed in 20 ml hexane with 0.14 mmol oleic acid and 0.152 mmol oleylamine inside. Then the solution was centrifuged to 6000 rpm for 10 min to eliminate the insoluble part, excessive ethanol was subsequently added into the solution to precipitate the nanoparticles, the solids were collected through centrifugation at 10 000 rpm for 10 min and dispersed in 20 ml hexane and used in the preparation of $Fe_3O_4$@$SiO_2$ core–shell nanoparticles.

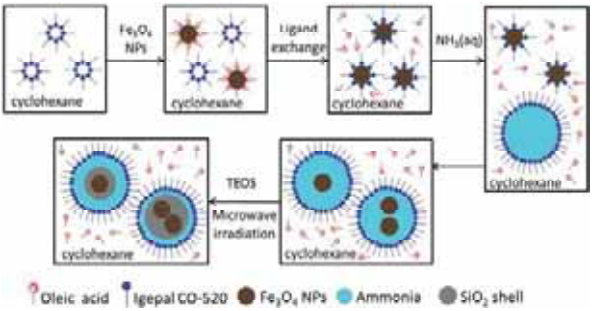


Fig. 1 Synthesis of $Fe_3O_4$@$SiO_2$ core–shell nanoparticles.

### Synthesis of $Fe_3O_4$@$SiO_2$ core–shell nanoparticles

In this process, different volume of Igepal CO-520 (1 ml, 1.5 ml, 2 ml corresponding to 200 mM, 300 mM, 400 mM in concentrations) were dissolved in 10 ml cyclohexane and stirred for 30 min, then 0.36 ml of as prepared $Fe_3O_4$ nanoparticles solution was added into the solution and stirred for 3 h followed by adding a variety concentration of ammonium hydroxide solution (71 mM, 141 mM, 211 mM and 280 mM) into the solution and kept stirring for 1 h to form a transparent water in oil (w/o) micro emulsion system. Finally the solution was mixed with 10 μl of tetraethyl orthosilicate in a microwave reaction vessel. The program was set as follows, the solution was stirred for 2 min in the first step then quickly heated up to 60 °C with the maximum operation power of 300 W and hold for 5 min, then cooled down to room temperature. The solid was precipitated by adding ethanol and washed with ethanol through centrifugation (10 000 rpm 10 min) for several times and finally the $Fe_3O_4$@$SiO_2$ core–shell nanoparticles were dispersed in 10 ml ethanol.

### Synthesis of $Fe_3O_4$@$SiO_2$/Ag nanocomposites

Before the decoration of Ag nanoparticles, the $Fe_3O_4$@$SiO_2$ core–shell nanoparticles were first functionalized with $-NH_2$ group. In a typical reaction 3 ml of synthesized core–shell nanoparticles suspension were diluted in 15 ml of distilled water with 0.1 ml of ammonia inside and ultrasound for 30 min, then 10 μl of (3-aminopropyl)triethoxysilane (APTES) was added into the solution follow by heating the mixture to 60 °C and keep stirring for 2 h. The nanoparticles were collected through centrifuge treatment (10 000 rpm, 30 min) and washed for several times with water and ethanol. Then disperse them in 20 ml water with ultrasound treatment for 30 min. After that, 0.5 ml of $AgNO_3$ aqueous solution (0.01 M) was added into the mixture with continues stirring in ice water bath, then 1 ml of $NaBH_4$ aqueous solution (0.01 M) was injected into the solution drop by drop to make a slowly formation of Ag nanoparticles. The mixture was stirred for another 2 h to get a black solution. Finally the $Fe_3O_4$@$SiO_2$/Ag nanocomposites were obtained through centrifuge (1000 rpm, 20 min) and washed several times with water and ethanol.

### Catalytic test

To study the catalytic properties of our synthesized $Fe_3O_4$@$SiO_2$/Ag nanocomposites, we use them in the reduction of 4-nitroaniline to 4-phenylenediamine. In a typical reaction, 400 μl of 1 mM 4-nitroaniline aqueous solution, 400 μl of 10 mM $NaBH_4$ aqueous solution and 200 μl of $Fe_3O_4$@$SiO_2$/Ag aqueous suspension were dispersed in 1 ml of $H_2O$. The reduction reaction was monitored through a UV-visible spectrophotometer in a quartz cuvette with 10 mm path length and with freshly made solutions. To study the recycling properties of $Fe_3O_4$@$SiO_2$/Ag nanocomposites, the exactly same process was repeated for 20 cycles. The nanoparticles were separated from the solution by simply applying a external magnetic field and washed for 2 times with distilled water for the following reduction reaction.

### Characterization methods

Fourier transform infrared spectroscopy (ATR-FT-IR) was performed on a Bruker Tensor[27] Fourier transform infrared spectrometer (Golden gate) in a range of 600–4000 $cm^{-1}$. All samples were measured in solid form at room temperature.

Transmission electron microscope (TEM) and high resolution transmission electron microscopy (HR-TEM) measurements were conducted on a JEOL 1210 TEM microscopy at 130 kv and a JEM-2011 HR-TEM microscopy at 200 kv. One drop of the hexane suspension of $Fe_3O_4$ nanoparticles and ethanol suspension of $Fe_3O_4$@$SiO_2$ and $Fe_3O_4$@$SiO_2$/Ag nanoparticles were deposited on the carbon-coated copper grids respectively. In order to minimize the aggregation of nanoparticles, the copper grids were laid on a filter paper during the drying process.

X-ray powder diffraction studies (XRD) were performed on D5000 Siemens X-ray powder diffractionmeter in a reflection mode by using Cu Kα $\lambda = 1.5406$ Å radiation in a range of $10^\circ \leq 2\theta \leq 80^\circ$.

The field-dependent magnetization curves were characterized by SQUID (Quantum design MPMS XL-7T) under a magnetic field from 0 to ±70 000 Oe at 5 K.

The thermogravimetric analysis (TGA) was carried on a NETZSCH-STA 449 F1 Jupiter thermal analysis system from room temperature to 800 °C under a $O_2$ flow.

Particle size distribution tests were implemented on a Zetasizer Nano Z system from Malvern Instruments (He–Ne laser 633 nm, Max 4 mW) by dynamic light scattering.

The catalytic reaction was characterized by a Varian Cary 5000 UV-Vis-NIR spectrophotometer operated at 1 nm resolution using freshly made solution in quartz cuvettes with 10 mm path length.

## Results and discussion

Fig. 3a and S1 (ESI†) display the TEM images of $Fe_3O_4$ NPs prepared using a modified previous published method.[38] The XRD measurements (Fig. 2) of both types of nanoparticles agree with the standard $Fe_3O_4$ XRD pattern (JCPDS no. 16-629) showing clearly the characteristic (220), (311), (400), (422), (511) and (440) diffraction peaks which also identify with the electron diffraction of $Fe_3O_4$ nanoparticles (Fig. S2, ESI†). The XRD pattern of $Fe_3O_4$@$SiO_2$ nanoparticles shows a wide peak around 20–25° which is ascribed to the amorphous silica shell, besides of this peak, the rest of diffraction peaks all belong to the characteristic peaks of the cubic structure of $Fe_3O_4$ nanoparticles.

In the FT-IR curve of $Fe_3O_4$ nanoparticles (Fig. 3b red line), the absorption peaks at 2192 $cm^{-1}$, 2850 $cm^{-1}$ are attributed to $-CH_2$ stretching vibration and 1708 $cm^{-1}$ is coming from C=O stretching modes of dimeric COOH groups and the peaks at 1406 $cm^{-1}$ could be ascribed to the coupling of hydroxyl bending vibration with C–O stretching vibration. The absorption band at 1598 $cm^{-1}$ is the characteristic peak of C=C vibration and the peak at 1522 $cm^{-1}$ is belonging to the $COO^-$ asymmetric stretching vibration. All those peaks indicate that

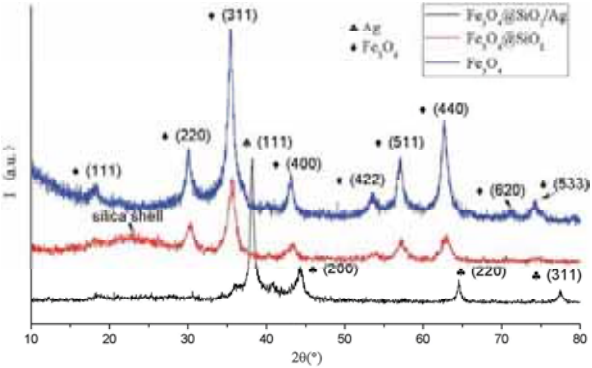


Fig. 2 XRD patterns of $Fe_3O_4$, $Fe_3O_4$@$SiO_2$ core–shell nanoparticles and $Fe_3O_4$@$SiO_2$/Ag nanocomposites.

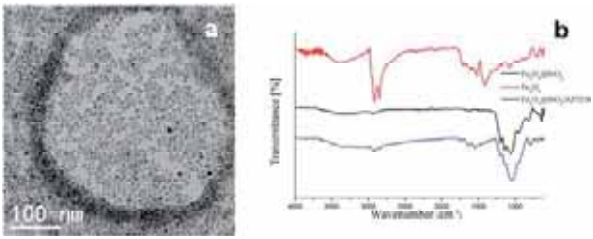


Fig. 3 TEM image of $Fe_3O_4$ NPs (a) and FT-IR curve of $Fe_3O_4$ nanoparticles, $Fe_3O_4$@$SiO_2$ core–shell nanoparticles and $Fe_3O_4$@$SiO_2$-APTES nanoparticles (b).

the oleic acid is absorbed on the $Fe_3O_4$ nanoparticles which results in a well dispersion of $Fe_3O_4$ in hexane. After the microwave irradiation, the FT-IR curve of $Fe_3O_4$@$SiO_2$ (Fig. 3b black line) shows two small peaks in 1512 $cm^{-1}$, 1457 $cm^{-1}$ coming from stretching vibration of aromatic ring C=C and two strong peaks in 1200 $cm^{-1}$ and 1060 $cm^{-1}$ which attribute to the symmetric stretching vibration of =C–O–C and asymmetric stretching vibration of =C–O–C. The existence of those vibration models indicates that there are still some amounts of Igepal CO-520 attached on the nanoparticles' surface. The absorption bands at 1145 $cm^{-1}$, 953 $cm^{-1}$, 819 $cm^{-1}$ attribute to the vibration models of $SiO_2$ which means that the $SiO_2$ were successfully covered on the $Fe_3O_4$ nanoparticles. The FT-IR results indicate the substitution of oleic acid and oleylamine capping ligands for the silica shell after microwave process. Strong bands centered at 820 $cm^{-1}$ can be unequivocally attributed to the vibration modes of $SiO_2$.

TEM studies of $Fe_3O_4$@$SiO_2$ core–shell nanoparticles prepared with microwave assistance and normal reverse microemulsion methods (Fig. 4a and b) prove that the core–shell structure is obtained through both methods but the size of

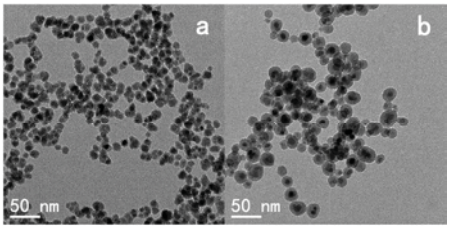


Fig. 4 TEM images of $Fe_3O_4$@$SiO_2$ core–shell nanoparticles prepared by microwave irradiation (a) and normal reverse microemulsion process (b).

samples are significantly different: the shell thickness is 6.6 nm and total size is about 30 nm for the normal reverse microemulsion method, on the other hand the shell is only 2.5 nm thick and total size is about 14 nm for the microwave assisted reaction. The thinner shell of microwave irradiation method could be ascribed to the short irradiation time during the TEOS

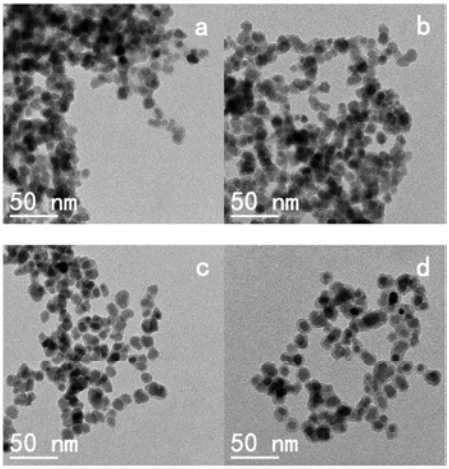


Fig. 5 TEM images of $Fe_3O_4$@$SiO_2$ nanoparticles synthesized by microwave assisted reverse microemulsion method with different concentration of ammonia inside, 71 mM (a), 141 mM (b), 211 mM (c) and 280 mM (d).

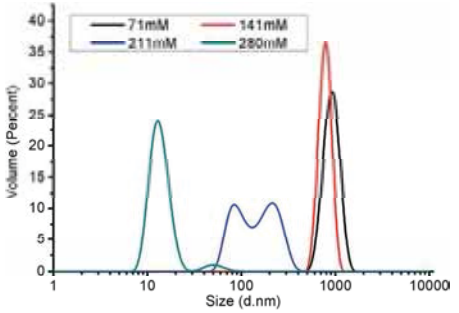


Fig. 6 Particle size distribution of $Fe_3O_4$@$SiO_2$ core–shell nanoparticles prepared under different concentration of ammonia.

Table 1 Shell thickness of $Fe_3O_4$@$SiO_2$ core–shell nanoparticles prepared with different concentration of ammonia

| Concentration of ammonia | 71 mM | 141 mM | 211 mM | 280 mM |
|---|---|---|---|---|
| Shell thickness | 2.51 nm | 2.55 nm | 2.54 nm | 2.60 nm |

hydrolysis reaction. It is worth to mention that the synthesized core–shell nanoparticles are not porous which made them unable combine the multifunctional capping agents with highly loading percentage compare to the recent reports about mesoporous silica nanocarriers.[39,40]

In order to optimize the silica shell formation, different concentrations of ammonia (71 mM, 141 mM, 211 mM and 280 mM) were used in each reaction. The TEM images (Fig. 5a–d) of core–shell nanoparticles show that after the microwave process a 2–3 nm thickness shell was formed. As is presented in Fig. 4 ammonia concentrations up to 211 mM give dispersions of particles with a chain like structure. Progressive increase of the amount of ammonia produced an improvement the dispersion reaching monodisperse core–shell NPs with ammonia concentration to 280 mM (Fig. 5d). DLS studies (Fig. 6) indicate that the samples prepared by using 71 mM and 141 mM ammonia show big aggregation and the sample synthesized by adding 211 mM ammonia shows a mixture of relative small size nanoparticles and big size aggregation. When 280 mM ammonia was used in the reaction, the DLS result (Fig. 6) shows that most of core–shell nanoparticles are about 15 nm which is in agreement with TEM results (Fig. 5). This effect can be explained by the role of ammonia in decorating the condensed $SiO_2$ surface that results in a more negatively charged layer, leading to a better dispersion of $Fe_3O_4$@$SiO_2$ nanoparticles. It should be pointed out that in this method the increasing concentration of ammonia does not affect the shell thickness of nanoparticles (see Table 1), whereas the shell thickness were changed with different concentration of ammonia in conventional reverse microemulsion method (see Table S1, ESI†). This effect might come from the short reaction time and ammonia evaporation during the microwave irradiation. The controll of shell thickness is under study.

The effect of the amount of surfactant was also studied. Increasing the amount of surfactant (Igepal CO-520) in the reaction produced a progressive decrease of the number of nanoparticles in the core (see Fig. 7a–c) and finally single-core core–shell nanoparticles were achieved using 400 mM surfactant. Based on the chemical mechanism previously discussed by Wang *et al.*,[20] the molar ratio of water and surfactant (Igepal CO-520 in our case) is very important for the morphology and particle size of core–shell structures. The increase of water/surfactant ratio produces the increase of micelles size facilitating intermicellar nucleation processes. For this reason, there were more nanoparticles inside the core of the sample than the other samples when 200 mM of Igepal CO-520 was employed at the first step of micelle formation.

$Fe_3O_4$@$SiO_2$ core–shell nanoparticles prepared by microwave irradiation display a strong magnetism that allows their

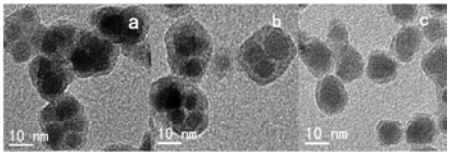


Fig. 7 TEM images of $Fe_3O_4$@$SiO_2$ core–shell nanoparticles prepared with different concentration of Igepal CO-520 inside, 200 mM (a), 300 mM (b) and 400 mM (c).

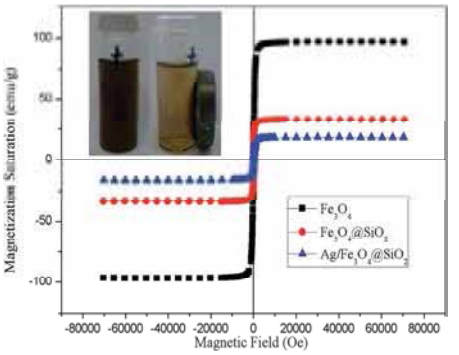


Fig. 8 Field-dependent magnetization curves (5 K) for the prepared $Fe_3O_4$, $Fe_3O_4$@$SiO_2$ core–shell and Ag/$Fe_3O_4$@$SiO_2$ nanoparticles measured by SQUID and a photo of Ag/$Fe_3O_4$@$SiO_2$ nanoparticles dispersed in water in the absence and presence of magnetic field (insert).

separation from the solution with a magnet. Fig. 8 shows the magnetization test of $Fe_3O_4$ and $Fe_3O_4$@$SiO_2$ core–shell nanoparticles. Magnetite nanoparticles are superparamagnetic with a high saturation magnetization value (96.9 emu $g^{-1}$). After covered by silica shell, the nanoparticles display a lower saturation magnetization (32.7 emu $g^{-1}$) but the core–shell structure remains superparamagnetic. Based on the calculation of weight percentage (ESI†) of $Fe_3O_4$ in the core–shell structure, the magnetization of $Fe_3O_4$ nanoparticles didn't change to nonmagnetic phase during the reaction. The magnetic properties of as prepared core–shell nanoparticles are comparable to other reported in the literature.[20]

The magnetic materials were widely used as the support for catalysis. For example, palladium catalysts were loaded on the Ni MOF-derived N-doped magnetic mesoporous carbon for the hydrodechlorination reaction of chlorophenols.[41] In this paper silver nanoparticles were synthesized on the surface of $Fe_3O_4$@$SiO_2$ core–shell nanoparticles. The obtained core–shell nanoparticles were first functionalized with $-NH_2$ group (see Fig. 3b blue line) by using APTES molecule. The weak absorption peaks between 1490 $cm^{-1}$ and 1631 $cm^{-1}$ and at 3352 $cm^{-1}$ attribute the $NH_2$ group of APTES and the peaks at 2922 $cm^{-1}$ and 2852 $cm^{-1}$ coming from the propyl chain of APTES molecule, all these peaks indicate the successful functionalization of $-NH_2$ group on the surface of core–shell nanoparticles. The silver nanoparticles were formed and decorated on the surface of silica shell through a simple reduction reaction. The XRD pattern of Ag/$Fe_3O_4$@$SiO_2$ nanocomposites (Fig. 2) indicates that strong diffraction peaks which identify with the standard Ag diffraction pattern (JCPDS no.04-0783) showing the characteristic (111), (200), (220) and (311) peaks. Fig. 9 shows the TEM images of Ag/$Fe_3O_4$@$SiO_2$ nanoparticles. From the images, the well-dispersed sliver nanoparticles were found to attach to the surface of core–shell nanoparticles with an average diameter

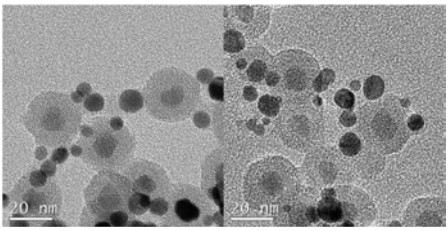


Fig. 9 TEM images of Ag/$Fe_3O_4$@$SiO_2$ nanoparticles.

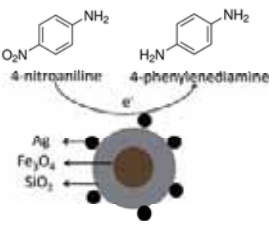


Fig. 10 Reaction mechanism about the reducing 4-nitroaniline when using Ag/$Fe_3O_4$@$SiO_2$ nanocomposites as the catalysts.

about 7 nm. It is noteworthy that the shell thickness of silica is thicker than the pictures in Fig. 7 which could be attributed to the process of functionalization the shell with APTES. The high angle annular dark-field scanning TEM (HAADF-STEM) image and corresponding elements mapping images (Fig. S5 ESI†), confirmed the Fe atoms were only distributed in the core and the Si atoms were homogeneously distributed around the $Fe_3O_4$ core, indicated a clearly core–shell structure. In the mean while the Ag atoms were main distributed outside the $SiO_2$ shell suggested a successfully decoration of Ag nanoparticles on the surface of $Fe_3O_4$@$SiO_2$ core–shell nanoparticles.

The decoration of silver nanoparticles on the $Fe_3O_4$@$SiO_2$ core–shell structure causes a further decrease in the magnetic saturation value to 18.2 emu $g^{-1}$ (Fig. 8), which was attribute to the mass effect of silver and silica. The Ag/$Fe_3O_4$@$SiO_2$ nanocomposites showed a strong magnetization which makes it separated by external magnetic field (see Fig. 8 insert image), indicates that this nanocomposites are suitable for magnetic separation and targeting.

The principal of the reduction reaction of 4-nitroaniline to 4-phenylenediamine when using Ag/$Fe_3O_4$@$SiO_2$ nanocomposite as the catalysis is showed in Fig. 10. This reaction is considered quite useful in the synthesis of rubber and polymer product[42,43] and the catalytic reduction of nitro-compound is well studied.[44] The whole reduction reaction could be easily monitored by the UV-vis spectroscopy through the decrease if the strong absorption peaks at 380 nm which could be attribute to 4-nitroanilinate anion. In the Fig. 11, a dramatically decreased of absorption peak at 380 nm when using Ag/$Fe_3O_4$@$SiO_2$ as the

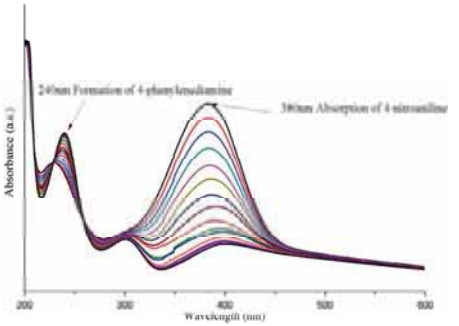


Fig. 11 UV-visible spectra for the reaction of 4-nitroaniline molecule by $Ag/Fe_3O_4@SiO_2$ nanocomposites at various times.

catalysis, meaning while a peak at 240 nm was appeared and getting stronger with the increase of reaction time which related to the 4-phenylenediamine. Based on the previous report, the reduction reaction happened through the transfer of electrons from the 4-nitroaniline molecules as long as both compounds attached on the surface of $Ag/Fe_3O_4@SiO_2$ nanocomposites. When the electron transferred to Ag nanoparticles the hydrogen atoms formed and attacked the 4-nitroaniline molecules leading to the occurrence of reduction reaction.[45] It is noteworthy that the 4-nitroaniline could be fully reduced within 5 min when using our synthesized $Ag/Fe_3O_4@SiO_2$ nanocomposites as the catalysis. This phenomenon could be explained by the high surface activity of Ag nanoparticles and the large surface area provided by the small size core–shell nanoparticles. These two characters ensure the $Ag/Fe_3O_4@SiO_2$ nanocomposites have a good catalytic property. And the TOF value was also calculated to 6 $h^{-1}$.

Another advantage of our synthesized $Ag/Fe_3O_4@SiO_2$ nanocomposite is high recyclability compared to the single Ag nanoparticles catalysts. The recycling test of $Ag/Fe_3O_4@SiO_2$ catalysis demonstrated that about 86% of 4-nitroaniline was reduced even after 20 cycles (see Fig. 12). It is worth to note that the nanoparticles start to aggregate after 20 cycles (Fig. S6†) and there were still many Ag nanoparticles located outside the aggregates. The unique core–shell structure makes the nanocomposites highly stable and easily separated by magnet results in a quite well reutilization property compared to other similar studies.[46]

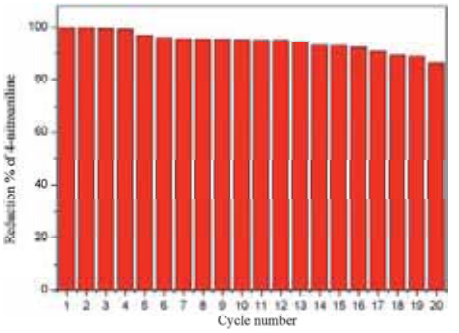


Fig. 12 The recycling curves of the catalyst $Fe_3O_4@SiO_2/Ag$ for 20 repetitions.

## Conclusions

A novel combination of reverse microemulsion system with microwave irradiation route was developed to prepare monodispersed $Fe_3O_4@SiO_2$ core–shell nanoparticles with a core–shell structure in a very short time. The magnetic nanoparticles were coated by a very thin layer of $SiO_2$ and the dispersity can be controlled by changing the volume of ammonia. On the other hand the number of nanoparticles inside the core could be tuneable through varying the concentration of surfactant (Igepal CO-520). Core–shell nanoparticles were superparamagnetic with a magnetization saturation value of *ca.* 32% of pure magnetite nanoparticles and the $Fe_3O_4@SiO_2$ nanoparticles were decorated by Ag nanoparticles. The produced $Ag/Fe_3O_4@SiO_2$ nanocomposites show nice catalytic efficiency and recycling property up 83% reduction of 4-nitroaniline after 20 cycles. This kind of core–shell structure materials can be also used in biomedical detection, drug delivery and battery system. It is also reasonable to believe that this new stagey is promising in rapid and massive production of various core–shell structure nanoparticles due to its time saving, facile and reliable properties.

## Acknowledgements

This work was supported by an EU project (Eurotapes, FP7/2007-2013 NMP3-LA2012-280432) and Generalitat de Catalunya (Pla de Recerca 2009-SGR-770 and XaRMAE). We acknowledge the Universitat Autònoma de Barcelona and Institute of Materials Science of Barcelona (ICMAB) in particular Bernat Bozzo and Dr Judith Oro for helping in the characterization of the materials. A pre-doctoral fellowship from the China Scholarship Council is also acknowledged.

## Notes and references

1 S. Laurent, D. Forge, M. Port, A. Roch, C. Robic, L. V. Elst and R. N. Muller, *Chem. Rev.*, 2008, **108**, 2064.
2 J. M. Jeong, B. G. Choi, S. C. Lee, K. G. Lee, S. J. Chang, Y. K. Han, Y. B. Lee, H. U. Lee, S. Kwon, G. Lee, C. S. Lee and Y. S. Hun, *Adv. Mater.*, 2013, **25**, 6250.
3 J. Fang, B. Zhang, Q. Yao, Y. Yang, J. Xie and N. Yan, *Coord. Chem. Rev.*, 2016, **322**, 1.
4 J. Qu, F. Ye, D. Chen, Y. Feng, Q. Yao, H. Liu, J. Xie and J. Yang, *Adv. Colloid Interface Sci.*, 2016, **230**, 29.
5 L. Liu, F. Ni, J. Zhang, X. Jiang, X. Lu, Z. Guo and R. Xu, *Acta Biochim. Biophys. Sin.*, 2011, **43**, 316.

6 L. Wang, J. Luo, S. Shan, E. Crew, J. Yin and C. O. Zhang, *Anal. Chem.*, 2011, **83**, 8688.
7 P. Zhang, C. Shao, Z. Zhang, M. Zhang, J. Mu, Z. Guo and Y. Liu, *Nanoscale*, 2011, **3**, 3357.
8 G. C. Rajib and P. Santanu, *Chem. Rev.*, 2011, **112**, 2373.
9 L. Z. Tong, J. H. Shi, D. M. Liu, Q. H. Li, X. Z. Ren and H. Yang, *J. Phys. Chem. C*, 2012, **116**, 7153.
10 J. H. Shen, Y. H. Zhu, X. L. Yang, J. Zong and C. Z. Li, *Langmuir*, 2012, **29**, 690.
11 V. M. Masalov, N. S. Sukhinina, E. A. Kudrenko and G. A. Emelchenko, *Nanotechnology*, 2011, **22**, 275718.
12 H. Mohammad-Beigi, S. Yaghmaei, R. Roostaazad, H. Bardania and A. Arpanaei, *Phys. E*, 2011, **44**, 618.
13 B. Q. Lu, Y. J. Zhu, G. F. Cheng and Y. J. Ruan, *Mater. Lett.*, 2013, **104**, 53.
14 J. Zou, Y. G. Peng and Y. Y. Tang, *RSC Adv.*, 2014, **4**, 9693.
15 X. M. Ni, Z. Zheng, X. K. Xiao, L. Huang and L. He, *Mater. Chem. Phys.*, 2010, **120**, 206.
16 W. Stöber, A. Fink and E. Bohn, *J. Colloid Interface Sci.*, 1968, **26**, 62.
17 T. Tago, T. Hatsuta, K. Miyajima, M. Kishida, S. Tashiro and K. Wakabayashi, *J. Am. Ceram. Soc.*, 2002, **85**, 2188.
18 J. Lee, Y. Lee, J. K. Youn, H. B. Na, T. K. Yu, H. Kim, S. M. Lee, Y. M. Koo, J. H. Kwak and H. G. Park, *Small*, 2008, **4**, 143.
19 C. Vogt, M. S. Toprak, M. Muhammed, S. Laurent, J. L. Bridot and R. N. Müller, *J. Nanopart. Res.*, 2010, **12**, 1137.
20 J. Wang, Z. H. Shah, S. Zhang and R. Lu, *Nanoscale*, 2014, **6**, 4418.
21 F. Jiang, Y. Fu, Y. Zhu, Z. K. Tang and P. Sheng, *J. Alloys Compd.*, 2012, **543**, 43.
22 S. Santra, R. Tapec, N. Theodoropoulou, J. Dobson, A. Hebard and W. Tan, *Langmuir*, 2001, **17**, 2900.
23 X. Gao, K. M. K. Yu, K. Y. Tam and S. Chi Tsang, *Chem. Commun.*, 2003, **24**, 2998–2999.
24 A. Guerrero-Martínez, J. Pérez-Juste and L. M. Liz-Marzán, *Adv. Mater.*, 2010, **22**, 1182.
25 M. Zhang, B. L. Cushing and C. J. O'Connor, *Nanotechnology*, 2008, **19**, 085601.
26 Y. Zhu, F. Y. Jiang, K. Chen, F. Kang and Z. K. Tang, *J. Sol–Gel Sci. Technol.*, 2013, **66**, 180.
27 H. L. Ding, Y. X. Zhang, S. Wang, J. M. Xu, S. C. Xu and G. H. Li, *Chem. Mater.*, 2012, **24**, 4572.
28 M. T. C. Fernandes, R. B. R. Garcia, C. A. P. Leite and E. Y. Kawachi, *Colloids Surf., A*, 2013, **422**, 136.
29 F. Chen, W. Bu, Y. Chen, Y. Fan, Q. He, M. Zhu, X. Liu, L. Zhou, S. Zhang and W. Peng, *Chem.–Asian J.*, 2009, **4**, 1809.
30 C. O. Kappe, *Angew. Chem., Int. Ed.*, 2004, **43**, 6250.
31 D. Dallinger and C. O. Kappe, *Chem. Rev.*, 2007, **107**, 2563.
32 Y. J. Zhu and F. Chen, *Chem. Rev.*, 2014, **114**, 6462.
33 C. Stutz, I. Bilecka, A. F. Thunemann, M. Niederberger and H. G. Borner, *Chem. Commun.*, 2012, **48**, 7176.
34 J. C. Park, D. A. Gilbert, K. Liub and A. Y. Louie, *J. Mater. Chem.*, 2012, **22**, 8449.
35 J. W. Doolittle Jr and P. K. Dutta, *Langmuir*, 2006, **22**, 4825.
36 K. L. M. Taylor, W. J. Rieter and W. Lin, *J. Am. Chem. Soc.*, 2008, **130**, 14358.
37 Z. Chen, S. Li and Y. Yan, *Chem. Mater.*, 2005, **17**, 2262.
38 S. H. Sun, H. Zeng, D. B. Robinson, S. Raoux, P. M. Rice, S. X. Wang and G. X. Li, *J. Am. Chem. Soc.*, 2004, **126**, 273.
39 T. Zhao, N. Goswami, J. Li, Q. Yao, Y. Zhang, J. Wang, D. Zhao and J. Xie, *Small*, 2016, DOI: 10.1002/smll.201601420.
40 S. Yang, D. Chen, N. Li, Q. Xu, H. Li, F. Gu, J. Xie and J. Lu, *Small*, 2016, **12**, 360.
41 X. Cui, W. Zuo, M. Tian, Z. Dong and J. Ma, *J. Mol. Catal. A: Chem.*, 2016, **423**, 386.
42 L. H. Shu and L. Y. Wen, *Ann. Occup. Hyg.*, 2009, **53**, 289.
43 I. Yoshiaki and K. Massaaki, *J. Health Sci.*, 2000, **46**, 467.
44 M. Tian, X. Cui, C. Dong and Z. Dong, *Appl. Surf. Sci.*, 2016, **390**, 100.
45 B. Naik, S. Hazra, V. S. Prasad and N. N. Chosh, *Catal. Commun.*, 2011, **12**, 1104.
46 H. Woo, K. Lee, S. Park and K. H. Park, *Molecules*, 2014, **19**, 699.

# Electronic Supporting Information

Ultra-fast microwave assistance reverse microemulsion synthesis of $Fe_3O_4$@$SiO_2$ core-shell nanoparticles as a highly recyclable silver nanoparticles catalytic platform in the reduction of 4-nitroaniline

**Journal:** RSC Advances

**Corresponding Authors:** C.Y.Lu[a,b]

**Other Authors:** T. Puig[b], X. Obradors[b], S. Ricart[b] and J. Ros[a]

**Address:**

a. Departament de Quimica，Edifici C Facultat de Ciències, Universitat Autònoma de Barcelona （UAB）, Cerdanyola del Vallès, Barcelona 08193, Spain. E-mail: lu.changyong@e-campus.uab.cat

b. Institute of Materials Science of Barcelona (ICMAB-CSIC), Campus de la UAB, Cerdanyola del Vallès, Barcelona 08193, Spain. E-mail: ricart@icmab.es

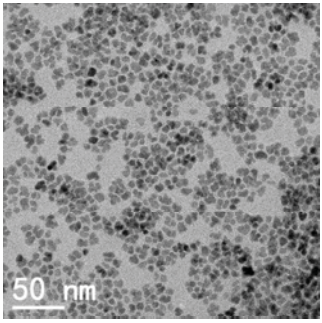


Figure S1. TEM overview of $Fe_3O_4$ nanoparticles.

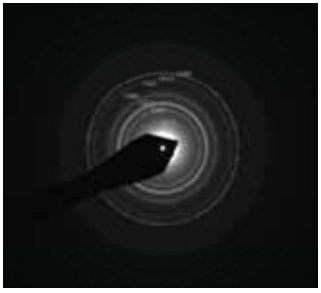

Figure S2. Electron diffraction of $Fe_3O_4$ nanoparticles.

Figure S1 indicates that the synthesized $Fe_3O_4$ nanoparticles are highly dispersed in hexane with a narrow size distribution and the average diameter is about 8nm. The electron diffraction pattern shows that the nanoparticles are well crystallized and has a good agreement with X-Ray diffraction results (Figure 2).

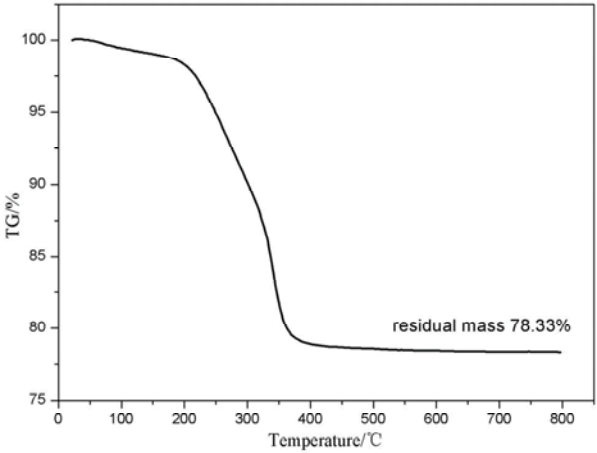


Figure S3. Thermogravimetric analysis of $Fe_3O_4$ nanoparticles.

| Concentration of ammonia | 71mM | 141mM | 211mM | 280mM |
|---|---|---|---|---|
| Shell thickness | 2.3nm | 4.2nm | 4.4nm | 6.6nm |

Table S1. Shell thickness of $Fe_3O_4$@$SiO_2$ core-shell nanoparticles prepared with different concentration of ammonia without microwave irradiation.

From Table S1, the increase of ammonia had great impact on the shell thickness; this is because with a higher concentration of ammonia the system form a larger size of micelle makes it possible to have more space to from silica shell in one core-shell nanoparticles.

**Weight percentage calculation of $Fe_3O_4$ in core-shell structure**

In order to justify whether magnetite materials were changed or not during the reaction, the weight percentage of $Fe_3O_4$ in core-shell structure was calculated based on the following assumption and equation (1). Since the sample prepared by using 200mM Igepal CO-520 and

280mM ammonia (TEM image corresponds to Figure 6a), there are more than one $Fe_3O_4$ nanoparticles inside the core-shell structure and there are still some $SiO_2$ exists between the $Fe_3O_4$ nanoparticles, the whole system could be seen as each $Fe_3O_4$ nanoparticle were covered by $SiO_2$ forming core-shell structure with only one core inside (see Figure S5).

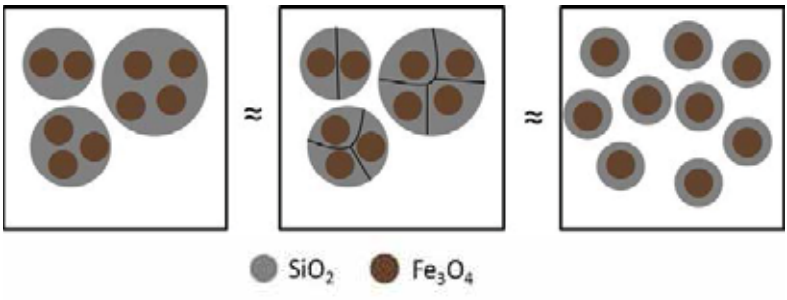


Figure S4. Assumption of core-shell nanoparticles with multicore inside

$$W = \frac{\frac{4}{3}\pi R_1^3 \times \rho_{Fe_3O_4}}{\left[\frac{4}{3}\pi(R_1+d)^3 - \frac{4}{3}\pi R_1^3\right] \times \rho_{SiO_2} + \frac{4}{3}\pi R_1^3 \times \rho_{Fe_3O_4}} \times 100\% \qquad \text{Equation (1)}$$

$R_1$: Average radius of $Fe_3O_4$ nanoparticles measured through TEM images (4.1nm).

d: Average shell thickness of the sample prepared with 200mM Igepla CO-520 and 280mM ammonia, measured by TEM images (3.2nm)

$\rho_{Fe_3O_4} = 5.17 g/cm^3$

$\rho_{SiO_2} = 2.2 g/cm^3$

According to equation (1), the weight percentage of $Fe_3O_4$ was calculated to 33.6%. The theoretical magnetization saturation of $Fe_3O_4$ nanoparticles could be calculated to 97.2emu/g by using the magnetization saturation of core-shell nanoparticles (32.7emu/g) divided by the weight percentage of $Fe_3O_4$ (33.6%), which is slightly larger than the real magnetization saturation of $Fe_3O_4$ measured by SQUID (96.9emu/g). This could be due to the overestimate of the percentage of $SiO_2$ in the system, since there are $Fe_3O_4$ nanoparticles stack together in some core-shell nanoparticles. The calculation indicates that the magnetization $Fe_3O_4$ nanoparticles didn't change during the reaction.

**Element distribution test**

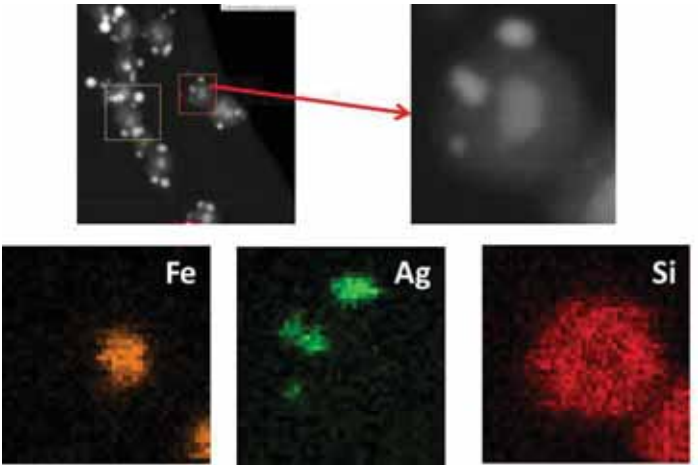


Figure S5. High angle annular dark-field scanning TEM (HAADF-STEM) image and corresponding elements mapping images of synthesized Ag/$Fe_3O_4$@$SiO_2$ nanoparticles.

The high angle annular dark-field scanning TEM (HAADF-STEM) image and corresponding elements mapping images (Figure S5) indicated that the Fe atoms were only distributed in the core and the Si atoms were homogeneously distributed around the $Fe_3O_4$ core suggested a clearly core-shell structure. From the element mapping image of silver, the Ag atoms were main distributed outside the $SiO_2$ shell revealed a successfully decoration of Ag nanoparticles on the surface of $Fe_3O_4$@$SiO_2$ core-shell nanoparticles.

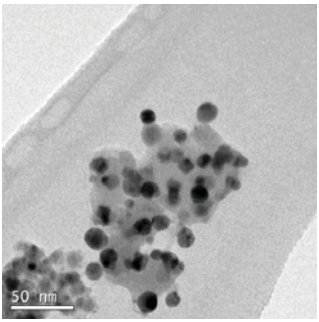


Figure S6 TEM image of Ag/$Fe_3O_4$/$SiO_2$ nanoparticles after 20 times repetitions of catalytic reaction.

The TEM image of Ag/$Fe_3O_4$/$SiO_2$ nanoparticles after 20 times repetitions of catalytic

reaction revealed that the nanoparticles start to aggregate after the catalytic reaction, during the formation of aggregation, some Ag nanoparticles are covered by $SiO_2$ layer and located inside the aggregates leading to the decreasing of catalytic property. But, it is worth to note that there were still many Ag nanoparticles located outside the aggregates, which guarantee a relatively high catalytic efficiency even after 20 times repetitions.

[1] S. H. Sun, H. Zeng, D. B. Robinson, S. Raoux, P. M. Rice, S. X. Wang and G. X. Li, *J. Am. Chem. Soc.*, 2004, 126(1): 273.